Control of the circular cylinder wake by Trust-Region methods and POD Reduced-Order Models

Michel Bergmann, Laurent Cordier

INSTITUT NATIONAL DE RECHERCHE EN INFORMATIQUE ET EN AUTOMATIQUE

Control of the circular cylinder wake by Trust-Region methods and POD Reduced-Order Models

Michel Bergmann — Laurent Cordier

N° 6552

Juin 2008

Thème NUM

ISSN 0249-6399 ISRN INRIA/RR--6552--FR+ENG

INSTITUT NATIONAL
DE RECHERCHE
EN INFORMATIQUE
ET EN AUTOMATIQUE

INRIA

centre de recherche
BORDEAUX - SUD OUEST

Control of the circular cylinder wake by Trust-Region methods and POD Reduced-Order Models

Michel Bergmann*, Laurent Cordier†

Thème NUM — Systèmes numériques
Équipe-Projet MC2

Rapport de recherche n° 6552 — Juin 2008 — 55 pages

Abstract: In this report we investigate the optimal control approach for the active control of the laminar circular cylinder wake flow (Re = 200). The objective is the minimization of the mean total drag where the control function is the time harmonic angular velocity of the rotating cylinder. When the Navier-Stokes equations are used as state equations, the discretization of the optimality system leads to large scale discretized optimization problems that represent a tremendous computational task. In order to reduce the number of state variables during the optimization process, a Proper Orthogonal Decomposition (POD) Reduced-Order Model (ROM) is then derived to be used as state equation. Since the range of validity of the POD ROM is generally limited to the vicinity of the design parameters in the control parameter space, we propose to use the Trust-Region Proper Orthogonal Decomposition (TRPOD) approach to update the reduced-order models during the optimization process. Benefiting from the trust-region philosophy, rigorous convergence results guarantee that the iterates produced by the TRPOD algorithm will converge to the solution of the original optimization problem defined with the Navier-Stokes equations. A lot of computational work is indeed saved because the optimization process is now based only on low order models. The key enablers to an accurate and robust POD ROM for the pressure and velocity fields are the extension of the POD basis functions to the pressure data, the introduction of eddy-viscosity estimated for each POD mode as the solution of an auxiliary optimization problem, and the inclusion of different non-equilibrium modes. When the TRPOD algorithm is applied to the wake flow configuration, this approach converges to the minimum predicted by an open-loop control approach and leads to a relative mean drag reduction of 30% for reduced numerical costs.

Key-words: Model reduction, Proper Orthogonal Decomposition, Surrogate optimization, Adaptive strategy

* Equipe Modélisation, Contrôle et Calcul (MC2) - Michel.Bergmann@inria.fr
† Laboratoire d'Etudes Aérodynamiques (Université de Poitiers, ENSMA, CNRS) 43, rue de l'Aérodrome 86036 Poitiers cedex, France - Laurent.Cordier@univ-poitiers.fr

Centre de recherche INRIA Bordeaux – Sud Ouest
Domaine Universitaire - 351, cours de la Libération 33405 Talence Cedex
Téléphone : +33 5 40 00 69 00

Contrôle optimal par réduction de modèle POD et méthode à région de confiance du sillage d'un cylindre circulaire

Résumé : Une approche de type contrôle optimal est appliqué à l'écoulement autour d?un cylindre de section circulaire (Re= 200). L'objectif est de minimiser par rotation la traînée moyenne en temps du sillage. Afin de réduire le nombre de variables d'état du système optimal, un modèle réduit de dynamique construit par POD (Proper Orthogonal Decomposition) est déterminé pour être utilisé comme équation d'état. Le domaine de validité du modèle POD étant généralement limité à un voisinage des paramètres de design, nous proposons d'appliquer l'algorithme TRPOD (Trust Region Proper Orthogonal Decomposition) pour renouveler le modèle réduit pendant la résolution du problème d'optimisation. Bénéficiant de résultats issus des méthodes à région de confiance, des preuves de convergence établissent que les itérés produits par TRPOD convergent vers la solution du problème d'optimisation original. Les coûts numériques sont ainsi réduits de manière importante car le processus d'optimisation est maintenant basé uniquement sur des modèles réduits de dynamique.

Pour déterminer un modèle réduit POD précis et robuste représentatif des champs de vitesse et de pression, les éléments clés sont (i) l'extension des fonctions de base POD à la pression, (ii) l'introduction d'une viscosité tourbillonnaire optimale fonction du mode POD et éventuellement du temps, (iii) l'ajout dans le modèle réduit POD de modes privilégiés dits de non équilibre.

L'algorithme TRPOD converge vers le minimum prédit par ailleurs dans une approche de type boucle ouverte. 30% de réduction relative du coefficient de traînée est obtenu.

Mots-clés : Modèles d'ordre réduit, Décomposition Orthogonale aux valeurs Propres, Optimisation, fonction modèle, méthode adaptative

1 Introduction

1.1 Reduced-order models in optimization

During the last decade, the *optimal control theory* [1] has emerged as a new approach to solve active flow control and aerodynamic shape design problems. Indeed, these problems can be reduced [2] to the minimization or maximization of an objective functional $\mathcal{J}$ (drag or lift coefficients, concentration of pollutant, emitted noise, mixing, ...) according to n control or design parameters $\boldsymbol{c} = (c_1, c_2, \cdots, c_n)$ (unsteady blowing/suction velocities, heat flows, ...) under some constraints (Navier-Stokes equations, geometric constraints, ...). However, whatever the specific class of numerical methods generally considered (methods of descent type, stochastic methods), the computational costs (CPU and memory) related to the resolution of optimization problems are so important that they become unsuited to the applications of flow control for three-dimensional turbulent flows. The application in an immediate future of active control to complex flows is thus conditioned by the development of approximate models of the system [3]. The objective of these surrogate models [4] is to capture the essence of the physics of the controlled system while reducing the costs associated to the solution of the nonlinear state equations. As a result, there have been many studies devoted to the development of Reduced-Order Models (ROM) that serve as low-dimensional approximation models to the large-scale discretized Navier-Stokes equations [5, for a review of the different reduced-order modelling techniques]. The model reduction method discussed in this paper fall in the category of reduced basis approaches. For the reduced bases, a number of choices exist [6, for a presentation] : Lagrange basis, Hermite basis, Taylor basis, Proper Orthogonal Decomposition (POD) basis [7, 8], Krylov basis [9], Centroidal Voronoi Tessellations (CVT) basis [10], balanced POD basis [11], etc. Today, the most popular reduced-order modelling approach for complex systems in fluid mechanics is based on POD. This study is restricted to this case: we consider that the unsteady non-linear dynamics of the flow is modelled via a reduced-order model based on POD (POD ROM).

The POD (and other similar techniques of ROM) can be viewed as a method of information compression. Essentially, the POD algorithm try to remove "redundant" information (if any) from the data base. As a consequence, the ability of POD modes to approximate any state of a complex system is totally dependent of the information originally contained in the snapshot set used to generate the POD functions. Thus, a POD basis cannot contain more information than that contained in the snapshot set. The generation of "good" snapshot set is then crucial to the success of use of POD ROM approach in a bifurcation analysis [12, 13, 14] or more generally in an optimization setting. Since the POD basis is intrinsic to a particular flow, we need to give special attention to adapt the POD ROM (and the POD basis naturally) to changes in physics when the flow is altered by control. This central question is discussed in more details in [15] where two strategies are evidenced for use of POD ROM in an optimization setting. A first approach consists in distributing uniformly in the control parameter space the snapshot ensemble to be used for POD. However, in this case, a lot of runs of the high-dimensional code would be necessary to generate the snapshots and that more especially as the number of the control parameters is important. Therefore, developing systematic and rational methodologies for

generating good snapshots set is a critical enabler for effective reduced-order modelling, since a POD basis is only as good as the snapshot set used to generate it. Very recently, it was demonstrated in [10] that Centroidal Voronoi Tessellations could be one method of intelligent sampling in parameter space. Failing this, a simpler method to implement is to generate generalized POD functions by forcing the flow with an ad-hoc time-dependent excitation that is rich in transients [16]. The second approach consists of an adaptive method in which new snapshots are regularly determined during the optimization process when the effectiveness of the existing POD ROM to represent accurately the controlled flow is considered to be insufficient [17, 18, 19]. At this point, two key questions still remain:

1. How to decide automatically whether or not a POD ROM has to be adapted to a new flow configuration?

2. Can we demonstrate under certain conditions (which should ideally be most general as possible) that the optimal solution based on the POD ROM corresponds to a local optimizer for the original problem?

The main drawback of this second approach is that for adaptively updating a reduced basis during an optimization process, new solves of the high-dimensional approximations of the Navier-Stokes equations need to be done. Since these simulations are costly, this approach is not appropriate for real-time control flow.

1.2 A prototype of separated flows: the cylinder wake flow

Due to its simple geometry and its representative behavior of separated flows [20], the cylinder wake flow has been broadly studied this past decade to experiment some control methods that could be used later in more complex engineering configurations. The majority of these studies were motivated by the experiments of [21] where 80% of relative[1] mean drag reduction was empirically found at $Re = 15,000$ by unsteady rotary oscillation of the cylinder. This experimental work was followed by a series of numerical [22, 23, 24, 25, 26, 27, 28, 29, 30] and experimental investigations [31, 32, 33, 34]. Recently, due to the maturity of control theory, optimization methods and computational fluid dynamics, optimal and suboptimal approaches attracted increased attention in flow control setting [35, 36, 37]. For example, in [38, 39, 40] the optimal control theory was used with the two-dimensional Navier-Stokes equations as the state equation to control by rotary oscillation the unsteady wake of the cylinder (see table 3 for the characteristics of these approaches). An attractive element of the optimal control approach is the introduction of a cost functional which provides a quantitative measure of the desired objective. However, the very large computational costs (CPU and memory), involved in the resolution of the optimality system commonly used in the optimal control theory [2], prevent to solve routinely optimization problems based on the three-dimensional Navier-Stokes equations[2].

[1] Here, and in the following occurrences in the text, the relative mean drag reduction is defined as $\left(\langle C_D\rangle_T^{\text{unforced}} - \langle C_D\rangle_T^{\text{forced}}\right)/\langle C_D\rangle_T^{\text{unforced}}$ where $\langle C_D\rangle_T$, the mean temporal drag coefficient estimated over a finite horizon T, is defined in Eq. (8). The terms 'unforced' and 'forced' are used respectively for non-rotating and rotating cylinder.

[2] Two exceptions are the seminal work of [41] and the subsequent study of [42] where the optimal control theory is used to determine controls that reduce the drag of a turbulent flow in

For cutting down these numerical costs different approaches are possible [3, for a review]. One promising approach is to first develop POD ROM to approximate the fluid flow and then to optimize exactly the reduced-order models as it was already discussed in section 1.1. A general discussion of the use of approximation models in optimization can be found in [44]. In this study, we want to develop a low-cost optimal control approach for the drag minimization of the cylinder wake with rotary motion for control law (see Fig. 1). In addition, as opposed to what was made in [15], where the cost functional to be minimized was not the drag but a drag-related cost function (the turbulent kinetic energy contained in the wake), we will directly take here for cost functional the mean drag coefficient (viscous and pressure contributions). Then, to reduce as much as possible the computational costs associated to the present study, the flow is considered two-dimensional and in the laminar regime. However, the methodology presented here that consists of combining the optimal control approach and a POD ROM should easily be expanded to three-dimensional and turbulent flows.

In their numerical investigation of the controlled wake flow by rotary oscillation of the cylinder, Protas and Wesfreid [30] argued (see § 2.2 for numerical evidence and more explanations) that in the supercritical regime, the effectiveness of the control in terms of drag reduction increases with the Reynolds number. This important result was recently confirmed by a study of our group [45] which showed analytically that the power necessary to control the wake by unsteady rotation varied, for fixed values of the control parameters A and St_f, like the inverse of the square root of the Reynolds number. Therefore, since the wake flow remains two-dimensional up to a value of the Reynolds number approximately equal to 190 where a spanwise supercritical Hopf bifurcation occurs and where the three-dimensional effects appear [46, 47], the "optimal" value of the Reynolds number for our two-dimensional study is slightly lower than 200. However for facilitating the comparisons with the results of the literature, a Reynolds number of 200 is considered. According to the observations of [38], the control minimizing the drag generates vortices that are less energetic than those produced by the stationary cylinder. An energetic criterion seems to be well adapted to the investigation of drag reduction. Therefore, due to the energetic optimality of convergence of the POD basis [7, 8, 48], the choice of POD to develop a reduced-order model of the controlled unsteady flow seems to be well adapted. A similar approach was already considered in [16, 49] to control the wake flow at a supercritical Reynolds number of 100.

Finally, we need to choose between the two opposite strategies discussed at the end of section 1.1. If we want to develop active flow control method that can be used for real-time, on-line feedback control, our interest is to include in the snapshot set all the information needed during the optimization process or at least as much information as we can, and then to generate the reduced-order basis. Following this approach the POD functions are determined once for all at the beginning of the optimization process and no refresh is realized. This method was successfully applied to control the cylinder wake flow in [15]. It was demonstrated that an accurate and robust POD ROM can be derived using a snapshot ensemble for POD based on chirp-forced transients of the flow. More-

a three-dimensional plane channel simulated at $Re_\tau = 180$. More recently, an optimal control approach was used in [43] to reduce the sound generated by a two-dimensional mixing layer.

over, 25% of relative drag reduction was found when the Navier-Stokes equations were controlled using an harmonic control law deduced from the optimal solution determined with the POD ROM. However, the excitation used to determine the generalized POD functions lacks of justifications and, with this particular approach, there is no mathematical assurance that the optimal solution based on the POD ROM corresponds to a local optimizer for the high-fidelity model. The same remark can be made concerning the approaches presented in [17, 18] and [19]. Indeed, in these articles, a new POD ROM is determined when the control law does not evolve sufficiently with the previous model. With this strategy, there is not any proof that the control which is finally obtained is solution of the initial problem of optimization. Therefore, in this paper, we propose to use a specific adaptive method called Trust-Region Proper Orthogonal Decomposition (TRPOD) to update the reduced-order models during the optimization process. This approach, originally introduced by [50], benefits from the trust-region philosophy [51, for an introduction]. Then, rigorous convergence results guarantee that the iterates produced by the TRPOD algorithm will converge to the solution of the original optimization problem defined with the Navier-Stokes equations, the so-called global convergence[3] of the trust-region methods. Moreover, in [15], the POD basis used to derive the reduced-order models represented only velocities. Therefore, a drag-related cost functional characteristic of the wake unsteadiness was minimized. Since the pressure term contributes to approximately 80% of the total drag coefficient for a Reynolds number equal to 200, here, a pressure POD basis was determined (§ 6.1), allowing us to consider the total drag as objective functional in our optimal control approach (§ 6.3).

The main objective of this paper is to demonstrate in a simple flow control configuration that the use of the TRPOD algorithm can be successful to determine at least a local minimizer of the original problem. To supplement this main result, we will also give an estimate of the computational savings that can be obtained by a POD ROM based optimal control approach compared with the more "classical" approach where the Navier-Stokes equations are used for constraints [38, 39, 40]. Consequently in this study our main concern is not to determine the control law with the maximum energetic efficiency as it can be characterized for example by the Power Saving Ratio (PSR) [40, for a definition or hereafter in § 7.2.3]. As far as we know (see table 3), the work presented in [40] is the only one which considers for cost functional the sum of the drag power and the control power thus making it possible to determine an optimal solution that is by construction energetically efficient. In the other works, the cost of the control is not considered or at best as a regularization parameter. This discussion will be developed in section 7.2.3 where we compare the energetic efficiency of the different approaches.

This manuscript is organized as follows. Section 2 begins with the introduction of the generic controlled flow configuration and a description of the numerical method used to simulate the flow. In the next two subsections, the main physical characteristics of the wake flow under study are first presented (§ 2.2), then an open-loop control study of the cylinder wake is carried out

[3] Let us consider a general unconstrained optimization problem $\min_{\boldsymbol{c}\in\mathbb{R}^n} f(\boldsymbol{c})$. The global convergence result of the trust-region methods states [50, for example] that $\lim_{k\longrightarrow\infty} \|\nabla f(\boldsymbol{c}_k)\| = 0$ where k represents the index of a current iterate of the iterative method.

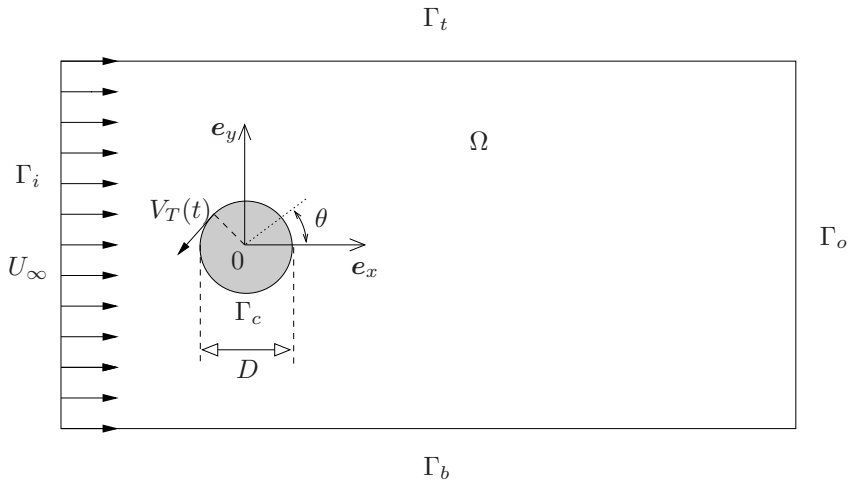

Figure 1: Controlled flow configuration.

(§ 2.3). Section 3 presents the Proper Orthogonal Decomposition (POD) while insisting on its main properties in terms of model reduction. The control function method, used in conjunction with the POD to develop an accurate POD Reduced-Order Model (POD ROM) of the controlled flow, is then described in § 4. The optimization by Trust-Region methods and POD Reduced-Order Models is presented in § 5 where the Trust-Region POD (TRPOD) algorithm is formally introduced. Following the philosophy of trust-region methods, a robust surrogate function for the mean drag coefficient is then constructed in § 6. The key enablers are the extension of the POD basis to the pressure field (§ 6.1) and the introduction of non-equilibrium modes in the POD expansion to represent different operating conditions (§ 6.2). Finally, we formulate an optimal control problem for the POD ROM (§ 7.1) and present the numerical results of the mean drag minimization of the cylinder wake flow obtained by a suboptimal and an optimal (TRPOD) POD-based adaptive controllers (§ 7.2).

2 Problem formulation and simulation method

2.1 Flow configuration, governing equations and numerical method

Let Ω be a two-dimensional bounded region filled with a Newtonian incompressible viscous fluid of kinematic viscosity ν and Γ denote the boundaries of Ω (Fig. 1). Wake flows dynamics are characterized [20] by the Reynolds number Re and by the natural Strouhal number St_n at which vortices are shed in the wake of the cylinder (Fig. 3). Traditionally, the Reynolds number is defined as $Re = U_\infty D/\nu$ where D is the cylinder diameter (R is the corresponding radius) and U_∞ the uniform velocity of the incoming flow. As for the natural Srouhal number, the common definition is $St_n = fD/U_\infty$ where f is the frequency characteristic of the periodic behavior of the flow. The rotary control is characterized by the instantaneous rotation rate $\dot{\theta}(t)$, or equivalently, by the non dimensional velocity $\gamma(t)$ defined as the ratio of the tangential velocity V_T to the upstream

velocity U_∞ *i.e.* $\gamma(t) = V_T(t)/U_\infty$. For $\gamma = 0$, the flow is said uncontrolled (natural flow). The objective of this study is the mean drag minimization of the wake flow by rotary oscillation of the cylinder as in the experiments of [21]. However, contrary to the case considered in [15] where no particular assumption was done on the variation of the control law, $\gamma(t)$ is hereafter sought using the optimal control theory as an harmonic function of the form:

$$\gamma(t) = A \sin(2\pi St_f t)$$

where the amplitude A and the *forcing* Strouhal number St_f correspond to two degrees of freedom for the control. Finally, for later notations convenience, we introduce the control vector $\boldsymbol{c} = (A,\, St_f)^T$.

The problem can be mathematically described by the incompressibility condition and the two-dimensional unsteady Navier-Stokes equations, where $\boldsymbol{u} = (u, v)$ is the velocity vector and p is the pressure:

$$\begin{cases} \boldsymbol{\nabla} \cdot \boldsymbol{u} = 0 \quad \text{in } \Omega \times [0,T]\,, \\ \dfrac{\partial \boldsymbol{u}}{\partial t} + \boldsymbol{\nabla} \cdot (\boldsymbol{u} \otimes \boldsymbol{u}) = -\boldsymbol{\nabla} p + \dfrac{1}{Re} \boldsymbol{\Delta} \boldsymbol{u} \quad \text{in } \Omega \times [0,T]\,, \end{cases} \tag{1}$$

subject to initial conditions

$$\boldsymbol{u}|_{t=0} = \boldsymbol{u_{IC}} \qquad \text{with } \boldsymbol{\nabla} \cdot \boldsymbol{u_{IC}} = 0\,, \quad \text{in } \Omega. \tag{2}$$

Those equations, and all variables in the following, are assumed to be non-dimensionalized with respect to the cylinder diameter D and the oncoming flow U_∞. $[0,T]$ corresponds to the time interval during which the flow is considered.

At the left boundary, an inflow boundary condition is applied:

$$(u, v) = (1, 0) \quad \text{on} \quad \Gamma_i \times [0,T]. \tag{3}$$

At the upper and lower boundaries, zero shear stress conditions are enforced:

$$\frac{\partial u}{\partial y} = 0\,, \quad v = 0 \quad \text{on} \quad \Gamma_b \times [0,T] \text{ and } \Gamma_t \times [0,T]. \tag{4}$$

At the outflow boundary, a non-reflecting boundary condition is considered. The velocity field is deduced on Γ_o as the solution of a wave-like equation [52]:

$$\frac{\partial \boldsymbol{u}}{\partial t} + u \frac{\partial \boldsymbol{u}}{\partial x} - \frac{1}{Re} \frac{\partial^2 \boldsymbol{u}}{\partial y^2} = \boldsymbol{0} \quad \text{on} \quad \Gamma_o \times [0,T]. \tag{5}$$

When this artificial boundary condition is used, no spurious reflections from the downstream boundary are observed thus making it possible to reduce the size of the computational domain.

Finally, on the cylinder surface the velocity is equal to the tangential boundary velocity:

$$\boldsymbol{u}(\boldsymbol{x}, t) = \gamma(t)\, \boldsymbol{e}_\theta(\boldsymbol{x}) \quad \text{on} \quad \Gamma_c \times [0,T]\,, \tag{6}$$

where $\boldsymbol{e}_\theta$ is the unit tangent vector on Γ_c.

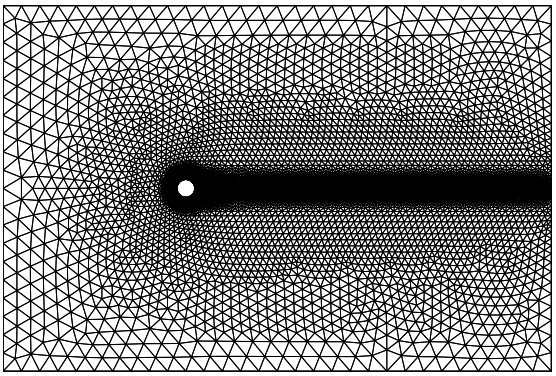

Figure 2: Finite-element mesh (diameter of the cylinder=1 ; upstream and downstream boundaries are respectively at 10 and 20 from the center of the cylinder ; height=20).

The partial differential equations (1) are discretized in time by a three-step projection method and in space using a Galerkin finite-element approximation (P_1, P_1). This numerical method is classic and the details that can be found in [53] will not be discussed here. The discrete equations are numerically solved on an unstructured mesh with the Partial Differential Toolbox of Matlab. The accuracy of the numerical code was extensively tested in [54] for different time steps, mesh sizes and Reynolds numbers varying from $Re = 4$ (creeping flow) to $Re = 1000$. It was shown that the code is second order accurate in space and first order accurate in time. The dependence of the mean drag coefficient and the natural Strouhal number on the Reynolds number were evaluated by comparison of reference results available in the literature. In particular, the well-known overprediction of the drag coefficient for two-dimensional simulations [20] was observed for values of the Reynolds number higher than about 180. Numerically, it was found that for a time step equal to $\Delta t = 1.5\,10^{-2}$ and a finite element mesh consisting of $25,000$ triangles and $12,686$ vertices (see Fig. 2), the present simulations described accurately the dynamics of the uncontrolled [54, for further validation] and controlled (§ 2.3) flows.

In a viscous flow the total forces acting on a body are contributed by the pressure and skin friction terms. Let $\boldsymbol{n}$ be the external normal vector to the boundary Γ_c, the aerodynamic coefficients are given by

$$\boldsymbol{C}(t) = -\int_{\Gamma_c} 2\,p\,\boldsymbol{n}\,d\Gamma + \frac{2}{Re}\int_{\Gamma_c}\frac{\partial \boldsymbol{u}}{\partial \boldsymbol{n}}\,d\Gamma = C_D(t)\,\boldsymbol{e}_x + C_L(t)\,\boldsymbol{e}_y\,, \tag{7}$$

where C_D and C_L represent respectively the drag and lift coefficients. For a circular cylinder, the mean time drag coefficient estimated over a finite horizon T equal to a few vortex shedding periods writes:

$$\langle C_D\rangle_T = \frac{1}{T}\int_0^T\int_0^{2\pi} 2\,p\,n_x\,R\,d\theta\,dt - \frac{1}{T}\int_0^T\int_0^{2\pi}\frac{2}{Re}\left(\frac{\partial u}{\partial x}\,n_x + \frac{\partial u}{\partial y}\,n_y\right)R\,d\theta\,dt\,, \tag{8}$$

where n_x and n_y are the projections of the vector $\boldsymbol{n}$ onto the cartesian basis vectors $\boldsymbol{e}_x$ and $\boldsymbol{e}_y$ respectively, and θ is an angle defining the curvilinear co-

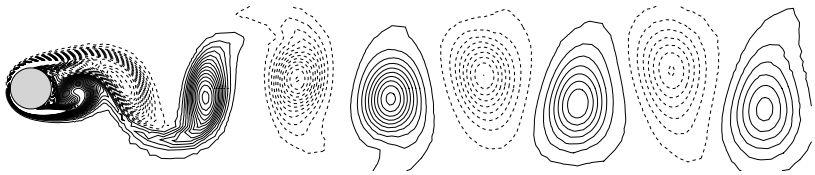

Figure 3: Vorticity contours for the uncontrolled flow ($\gamma = 0$) at time $t = 100$ and $Re = 200$ (dashed lines correspond to negative values).

Table 1: Comparison at $Re = 200$ of the natural vortex shedding Strouhal number and the mean total drag coefficient for our simulation and reference results.

Re	*Authors*	St_n	$\langle C_D \rangle_T$
200	[56]	0.2000	1.4000
	[57]	0.1971	1.3412
	[38]	0.1978	1.3560
	Present study	0.1999	1.3900

ordinate of a point on Γ_c. By convention, this angle is initialized at the front stagnation point of the cylinder (see Fig. 1).

2.2 Results of the simulation at $Re = 200$

In this section, we briefly present the main physical characteristics of the wake flow at a Reynolds number equal to 200 *i.e.* at the specific flow regime retained for our study. Additional information and other results of numerical simulations can be found in [15] or [54]. In Fig. 3, we present iso-vorticity contours of a typical long-term flow solution. Clearly, an alternative vortex shedding corresponding to the well-known Von Kármán street is visible. Two important characteristics of bluff body wakes are the natural frequency of vortex shedding and the time-averaged drag coefficient. In table 1, these values are compared with reference results available in the literature. The agreement with all the previous experimental and computational data is very good. Similarly (not shown in table 1), the time-averaged lift coefficient is seen to be in very good agreement with the results obtained previously. Likewise, in conformity with the recent results of [55], the spectra of the drag and lift forces are made up only of even and odd harmonics respectively.

Lastly, we conclude our presentation of the physical characteristics of the wake flow at $Re = 200$ by a discussion of the unstable symmetric state of the flow (see Fig. 21(c) for a representation). Let us recall [30, for example] that in the supercritical regime of the wake flow, every mean quantity consists of two terms, the *basic flow i.e.*, the unstable, steady, symmetric flow, and the *mean flow correction* which is due to the vortex shedding. Consequently, the mean time drag coefficient $\langle C_D \rangle_T$ writes:

$$\langle C_D \rangle_T = C_D^{basic} + C_D^{\Delta}\,, \tag{9}$$

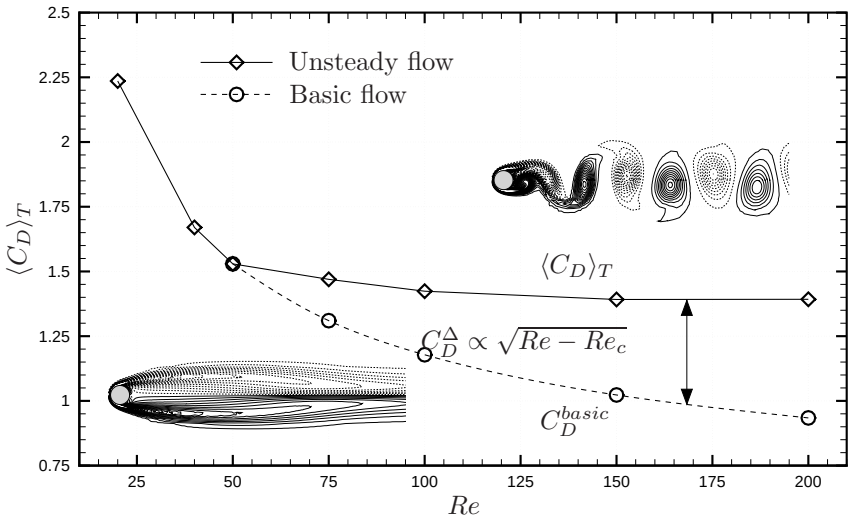

Figure 4: Variation with the Reynolds number of the mean drag coefficient. Contributions and corresponding flow patterns of the basic flow and unsteady flow.

where C_D^{basic} and C_D^{Δ} represent the drag of the basic flow and the mean flow correction respectively (see Fig. 4). The basic flow is determined with (almost) the same unsteady Navier-Stokes solver used to determine the stable flow by ensuring at every time step that the flow remains symmetric [15]. It can be shown numerically that the amplitude of C_D^{Δ} scales as the square root of the distance of the Reynolds number from the critical value Re_c corresponding to the steady/unsteady bifurcation (in our simulation $Re_c \simeq 46$). In fact, this behavior is not very surprising because it is a characteristic of the amplitude of the saturated state obtained after a Hopf bifurcation [20]. Of course, at a given Reynolds number, the contribution of the basic flow to drag cannot be modified. Then controlling the wake flow by rotary oscillations can only reduce the contribution of the mean flow correction to drag. If we assume as in [30] that the drag of the mean flow correction field can be only positive[4], the minimal value of drag that can be obtained under periodic forcing conditions is that corresponding to the basic flow. In conclusion, this flow would be thus a natural 'desired' field in a flow tracking procedure of optimization.

2.3 Open-loop control of the cylinder wake

The main results of an open-loop control study performed numerically to validate *a posteriori* the control law obtained with the optimization method based on the POD ROM are now summarized. As it was already mentioned in § 2.1, the active control of the cylinder is based on oscillatory rotation characterized by the forcing angular velocity $\gamma(t) = A \sin(2\pi St_f t)$. In order to analyze the

[4]Recently, numerical evidence were brought [58] that, for the circular cylinder wake flow at $Re = 200$, a partial control restricted to an upstream part of the cylinder surface could lead to a mean flow correction field with negative drag.

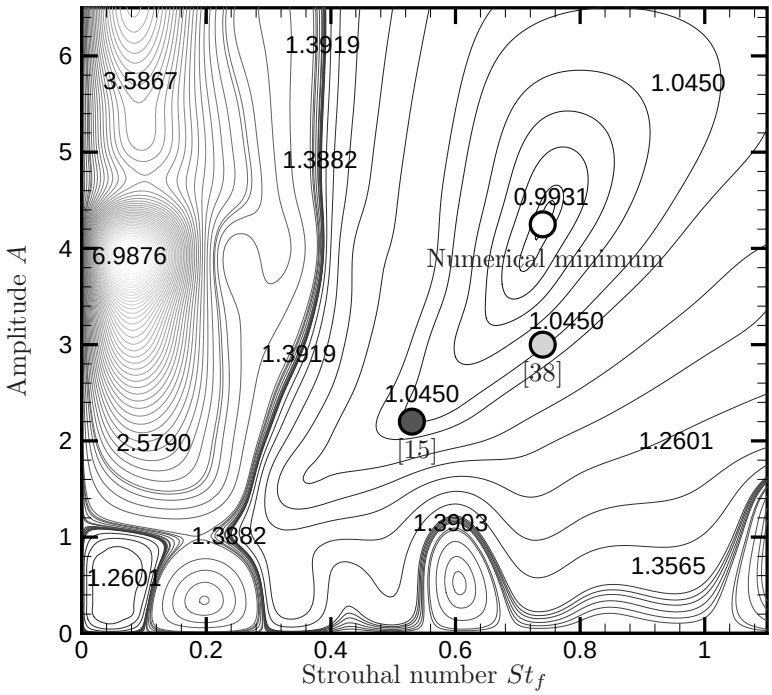

Figure 5: Variation of the mean drag coefficient with A and St_f at $Re = 200$. Numerical minimum: $(A_{min}, St_{f_{min}}) = (4.25, 0.74)$; [38]: $(A, St_f) = (3., 0.75)$; [39] (not shown): $(A, St_f) = (3.25, 1.13)$; [15]: $(A, St_f) = (2.2, 0.53)$.

influence of the forcing parameters A and St_f onto the mean drag coefficient, a series of simulations with different amplitude A varying from 0 to 6.5 by step of 0.5 and different forcing Strouhal number St_f varying from 0 to 1. by step of 0.1 was made. For a Reynolds number equal to 200, the forcing frequency St_f ranges from one-half to five natural shedding frequency St_n. For every forcing frequency our simulations are performed for a sufficient long time ($T_S = 130$) to assure that the saturated state has been reached. All simulations have been done with the same time step, here equal to $1.5\,10^{-2}$. In Fig. 5, we visualize the contours of the mean temporal drag estimated over the last 30 units of time in the space spanned by the forcing parameters A and St_f. In this figure, interpolations by spline functions were done between the values of mean drag coefficient obtained for the various control parameters. Numerically, the mean drag coefficient reaches a minimal value, which appears to correspond to a global minimum of the drag function on the domain studied, for an optimal pair $(A_{min}, St_{f_{min}}) = (4.25, 0.74)$. The corresponding minimum value is 0.99. It is noticeable that the function defined by the mean drag coefficient is rather regular, and that the minimum is located in a smooth valley. Another strik-

ing feature of this open-loop control study is that with the use of a sinusoidal control law on the whole cylinder the minimal value of the mean drag coefficient remains greater than that obtained for the basic flow ($\langle C_D^{basic} \rangle_T = 0.94$ at $Re = 200$) as it was argued by [30]. In other words, the value of the mean drag correction term $\langle C_D^{\Delta} \rangle_T$ is always positive.

3 The Proper Orthogonal Decomposition

The Proper Orthogonal Decomposition (POD), also known as Karhunen-Loève decomposition, principal component analysis or empirical eigenfunctions method, is a standard statistical pattern recognition and image compression technique that have been independently rediscovered several times. The reader is referred to a monograph by [59] and review articles by [8] and [48] for a comprehensive review of the POD. The fundamental idea of the POD is to look for the deterministic function $\boldsymbol{\phi}(\boldsymbol{x})$ that is most similar on average to the realizations $\boldsymbol{U}_{snap}(\boldsymbol{x}, t)$ contained in a set of realizations (velocity, pressure, temperature fields, etc). Here, since the data are issued from numerical simulations [48, for a justification], the snapshot POD introduced by [8] is adopted. In this case, the constrained optimization problem reduces to the following Fredholm integral eigenvalue problem:

$$\int_0^T C(t,t') a_n(t')\, dt' = \lambda_n a_n(t) \tag{10}$$

where $C(t,t')$ is the temporal correlation tensor constructed as

$$C(t,t') = \frac{1}{T} \left(\boldsymbol{U}_{snap}(\boldsymbol{x},t), \boldsymbol{U}_{snap}(\boldsymbol{x},t') \right)_{\Omega}. \tag{11}$$

The outer parentheses $(.,.)_{\Omega}$ represent the inner product between two fields $\boldsymbol{U}_{snap}$ and $\boldsymbol{V}_{snap}$. By definition, this product is estimated as:

$$(\boldsymbol{U}_{snap}, \boldsymbol{V}_{snap})_{\Omega} = \int_{\Omega} \boldsymbol{U}_{snap} \cdot \boldsymbol{V}_{snap}\, d\boldsymbol{x} = \int_{\Omega} \sum_{i=1}^{n_c} U_{snap}^i V_{snap}^i\, d\boldsymbol{x},$$

where $U_{snap}^i \, (i = 1, \cdots, n_c)$ represents the i^{th} component of $\boldsymbol{U}_{snap}$.

The eigenvalues λ_n $(n = 1, \ldots, +\infty)$ determined in (10) are all real and positive and form a decreasing and convergent series. Each eigenvalue represents the contribution of the corresponding mode $\boldsymbol{\phi}_n$ to the information content (total kinetic energy if $\boldsymbol{U}_{snap}$ are velocity fields) contained in the original data. If the decrease of the POD spectrum, as measured for example by the information content captured by the first N POD modes $\sum_{i=1}^{N} \lambda_i$, is fast enough than neglecting in the Galerkin approach the POD modes $\boldsymbol{\phi}_i$ for $i > N$ can lead to a reduced-order model of the original dynamics.

In Eq. (10), a_n are the time-dependent POD eigenfunction of order n. These modes form an orthogonal set, satisfying the condition:

$$\frac{1}{T} \int_0^T a_n(t) a_m(t)\ dt = \lambda_n \delta_{nm}. \tag{12}$$

The associated eigenvectors $\boldsymbol{\phi}_n$ (also called empirical eigenfunctions) form a complete orthogonal set and have been normalized, so that they verify $(\boldsymbol{\phi}_n, \boldsymbol{\phi}_m)_\Omega = \delta_{nm}$.

The spatial basis functions ϕ_n^i can then be calculated from the realizations U_{snap}^i and the coefficients a_n with:

$$\phi_n^i(\boldsymbol{x}) = \frac{1}{T\,\lambda_n} \int_0^T U_{snap}^i(\boldsymbol{x}, t) a_n(t)\ dt. \tag{13}$$

Since the POD eigenfunctions can be represented as linear combinations of the realizations, they inherit all the properties of the original data that are linear or homogeneous. Hence the eigenfunctions are divergence free for solenoidal realizations $\boldsymbol{U}_{snap}$. A common example is the case of incompressible fluid for which the POD is applied to velocity fields. Moreover, the eigenfunctions verify automatically the homogeneous boundary conditions of the numerical simulation used to determine the flow realizations.

The set of POD modes $\{\boldsymbol{\phi}_n\}_{n=1}^{+\infty}$ is complete in the sense that any realization $\boldsymbol{U}_{snap}(\boldsymbol{x}, t)$ contained in the original data set, can be expanded with arbitrary accuracy in the eigenfunctions as

$$\boldsymbol{U}_{snap}(\boldsymbol{x}, t) \simeq \widehat{\boldsymbol{U}}_{snap}^{[1,\cdots,N_{POD}]}(\boldsymbol{x}, t) = \sum_{n=1}^{N_{POD}} a_n(t)\boldsymbol{\phi}_n(\boldsymbol{x}) \tag{14}$$

where N_{POD} is equal to the number of flow realizations used to solve the POD problem (10). For later reference, the estimation $\widehat{\boldsymbol{U}}_{snap}^{[1,\cdots,N_{POD}]}$ of $\boldsymbol{U}_{snap}$ is introduced, where the brackets contain the indices of all employed modes.

Hereafter, we consider that the input ensemble used to determine the POD modes consists of N_t flow realizations called time snapshots $\boldsymbol{U}_{snap}(\boldsymbol{x}, t_i)$, $\boldsymbol{x} \in \Omega$, taken at time instants $t_i \in [0, T]$, $i = 1, \cdots, N_t$.

4 POD ROM of the controlled cylinder wake

When the cylinder is set into an oscillatory rotation, the boundary conditions on Γ_c become inhomogeneous and time dependent. Due to Eq. (13), the POD basis functions $\boldsymbol{\phi}_n$ do not satisfy homogeneous boundary conditions. However, having homogeneous boundary conditions on the basis functions used in the Galerkin projection is highly desirable to simplify the numerical evaluation of the POD ROM coefficients (see the boundary terms in Eq. 18). To overcome this difficulty, the *control function method* introduced in [16] is used.

4.1 The control function method

In this approach the inhomogeneous boundary conditions on Γ are removed through the introduction of a suitable control function $\boldsymbol{c}_f(\boldsymbol{x}, t)$ in the expansion (14) for the velocity field. To retain the divergence-free property of the POD basis functions, $\boldsymbol{c}_f(\boldsymbol{x}, t)$ must also be divergence-free. Here, the introduction of this control function is justified in the general context of boundary control problem for fluid flows where the boundary conditions are of Dirichlet type. Without any restriction, the boundary of the domain, Γ, can be split into

two parts such that Γ_c denotes that part of the boundary where the control is applied and $\Gamma \setminus \Gamma_c$ is the part of the boundary that is not controlled. For the need of the presentation, we consider[5] that for the controlled cylinder wake flow that is under study, all the boundary conditions on $\Gamma \setminus \Gamma_c$ are of Dirichlet type and independent of time. In a general way, they will be noted $\boldsymbol{f}(\boldsymbol{x})$ thereafter. The boundary conditions (3) to (6) can then be written as:

$$\boldsymbol{u}(\boldsymbol{x},t) = \begin{cases} \gamma(t)\boldsymbol{e}_\theta(\boldsymbol{x}) & \text{on } \Gamma_c \times [0,\, T]\,, \\ \boldsymbol{f}(\boldsymbol{x}) & \text{on } \Gamma \setminus \Gamma_c \times [0,\, T]. \end{cases} \tag{15}$$

In order to match these boundary conditions, the velocity field has to be expanded in

$$\boldsymbol{u}(\boldsymbol{x},t) = \boldsymbol{u}_m(\boldsymbol{x}) + \boldsymbol{c}_f(\boldsymbol{x},\, t) + \sum_{k=1}^{N_{POD}} a_k(t)\boldsymbol{\phi}_k(\boldsymbol{x})\,, \tag{16}$$

where $\boldsymbol{u}_m(\boldsymbol{x})$ is the mean velocity field computed as an ensemble average of the modified snapshot set $\{\boldsymbol{u}(\boldsymbol{x},t_i) - \boldsymbol{c}_f(\boldsymbol{x},\, t_i)\}_{i=1}^{N_t}$. A relevant way to define the control function is $\boldsymbol{c}_f(\boldsymbol{x},\, t) = \gamma(t)\,\boldsymbol{u}_c(\boldsymbol{x})$ where $\boldsymbol{u}_c(\boldsymbol{x})$ is a reference flow field called actuation mode that describes how the control action $\gamma(t)\boldsymbol{e}_\theta(\boldsymbol{x})$ influences the flow. The main interest of this definition is that the control law $\gamma(t)$ will appear explicitly in the POD Reduced-Order Model (see section 4.2) in a similar manner to what occur in the state-space models of linear dynamical systems [60]. Finally, the control function has to satisfy the boundary conditions:

$$\gamma(t)\boldsymbol{u}_c(\boldsymbol{x}) = \begin{cases} \gamma(t)\boldsymbol{e}_\theta(\boldsymbol{x}), & \text{on } \Gamma_c \times [0,\, T]\,, \\ \boldsymbol{0} & \text{on } \Gamma \setminus \Gamma_c \times [0,\, T]. \end{cases} \tag{17}$$

A convenient way to generate $\boldsymbol{u}_c(\boldsymbol{x})$ is to take the solution of the governing equations (1) for the steady cylinder rotation with angular velocity $\gamma = 1$ and homogeneous boundary conditions for the uncontrolled part of Γ (see Fig. 13(k) for a streamlines representation of $\boldsymbol{u}_c$).

To sum up, the procedure for computing POD basis functions with homogenized boundary conditions for a time-dependent controlled flow can be formulated as follows. First, a mean velocity field $\boldsymbol{u}_m(\boldsymbol{x})$ is computed as the ensemble average of the modified input data defined as $\mathcal{U}_m = \{\boldsymbol{u}(\boldsymbol{x},t_i) - \gamma(t_i)\boldsymbol{u}_c(\boldsymbol{x})\}_{i=1}^{N_t}$. Essentially, the role of $\boldsymbol{u}_m$ is to match all non homogeneous boundary conditions that are independent of time *i.e.* $(\boldsymbol{u}(\boldsymbol{x},t_i) - \boldsymbol{u}_m(\boldsymbol{x}))|_{\Gamma \setminus \Gamma_c} = \boldsymbol{0}$. This point explains why computing POD functions for the fluctuations around the mean flow field $\{\boldsymbol{u}(\boldsymbol{x},t_i) - \boldsymbol{u}_m(\boldsymbol{x})\}_{i=1}^{N_t}$ are also popular for the uncontrolled configurations. Finally, the POD basis functions $\boldsymbol{\phi}_n$ are estimated with the input collection $\mathcal{U}' = \{\boldsymbol{u}(\boldsymbol{x},t_i) - \gamma(t_i)\boldsymbol{u}_c(\boldsymbol{x}) - \boldsymbol{u}_m(\boldsymbol{x})\}_{i=1}^{N_t}$. Since $(\boldsymbol{u}(\boldsymbol{x},t_i) - \gamma(t_i)\boldsymbol{u}_c(\boldsymbol{x}))|_{\Gamma_c} = \boldsymbol{0}$, the POD basis functions $\boldsymbol{\phi}_n$ satisfy homogenized boundary conditions on the whole domain.

[5] In fact, the nonreflective boundary conditions imposed on the outflow Γ_o are dependent on time. On this boundary, and only on this one, the POD eigenfunctions will thus not be homogeneous after use of the control function method. As a consequence, it will be necessary to model in the POD ROM (19) the contributions coming from this boundary. This point is discussed in § 4.2.

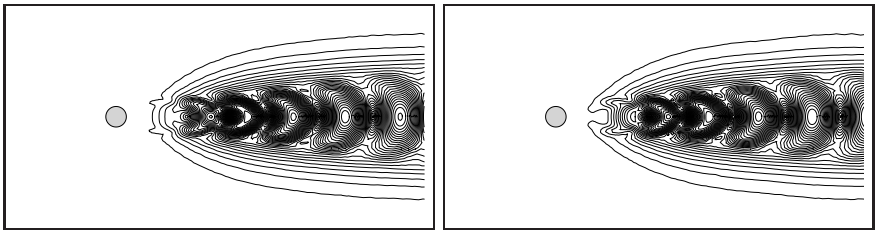

(a) mode 1. (b) mode 2.

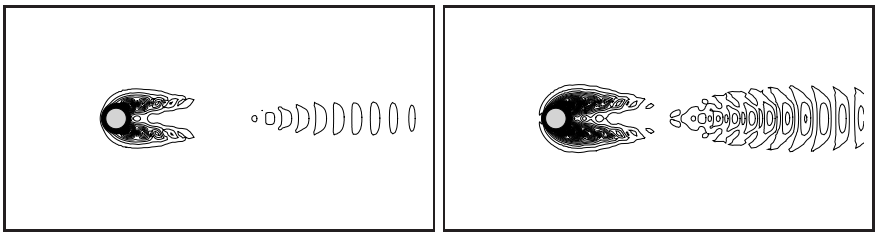

(c) mode 3. (d) mode 4.

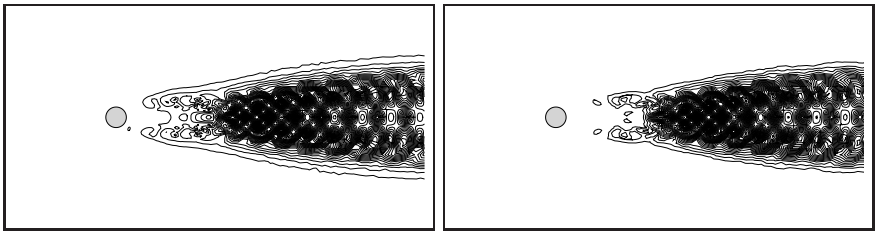

(e) mode 5. (f) mode 6.

Figure 6: Velocity POD basis functions for the controlled cylinder wake at $Re = 200$. The first six POD modes $\boldsymbol{\phi}_n$ are visualized by iso-contour lines of their norm ($\|\boldsymbol{\phi}_n\|_\Omega$) for $\gamma(t) = A\sin(2\pi St_f t)$ with $A = 2$ and $St_f = 0.5$.

As illustration, the first six POD basis functions computed from snapshots that are issued from numerical simulation of the controlled wake flow ($\gamma(t) = A\sin(2\pi St_f\, t)$ with $A = 2$ and $St_f = 0.5$) are displayed in Fig. 6.

4.2 Derivation of the POD ROM

The POD basis functions that were previously determined may now be used to generate a predictive model via a Galerkin projection of the Navier-Stokes equations (1). The principle consists to restrict the weak form of the Navier-Stokes equations to the subspace $\mathcal{S}^{POD}_{N_{gal}}$ spanned by the first N_{gal} spatial eigenfunctions $\boldsymbol{\phi}_i$. The energetic optimality of the POD basis functions suggests that only a very small number of POD modes may be necessary to describe efficiently any flow realizations of the input data *i.e.* $N_{gal} \ll N_{POD}$. In practice,

N_{gal} is usually determined as the smallest integer M such that the Relative Information Content, $RIC(M) = \sum_{i=1}^{M} \lambda_i / \sum_{i=1}^{N_{POD}} \lambda_i$, is greater than a predefined percentage of energy, δ. For the controlled wake flow characterized by $A = 2$ and $St_f = 0.5$, with 360 snapshots taken uniformly over $T_{snap} = 18$, the first 14 POD modes represent 99.9% of the total kinetic energy included in the data ensemble, *i.e* $N_{gal} = 14$ for $\delta = 0.999$. The Galerkin projection of the Navier-Stokes equations (1) onto the POD basis functions leads to [53]:

$$\left(\boldsymbol{\phi}_i,\, \frac{\partial \boldsymbol{u}}{\partial t} + (\boldsymbol{u}\cdot\boldsymbol{\nabla})\boldsymbol{u}\right)_\Omega = (p,\, \boldsymbol{\nabla}\cdot\boldsymbol{\phi}_i)_\Omega - \frac{1}{Re}\left(\boldsymbol{\nabla}\boldsymbol{\phi}_i,\, (\boldsymbol{\nabla}\boldsymbol{u})^T\right)_\Omega - [p\,\boldsymbol{\phi}_i]_\Gamma + \frac{1}{Re}\left[(\boldsymbol{\nabla}\boldsymbol{u})^T\boldsymbol{\phi}_i\right]_\Gamma \tag{18}$$

$$\text{with } [\boldsymbol{u}]_\Gamma = \int_\Gamma \boldsymbol{u}\cdot\boldsymbol{n}\; d\boldsymbol{x} \text{ and } \left(\overline{\overline{A}},\, \overline{\overline{B}}\right)_\Omega = \int_\Omega \overline{\overline{A}} : \overline{\overline{B}}\, d\boldsymbol{x} = \sum_{i,\,j=1}^{n_c} \int_\Omega A_{ij}B_{ji}\, d\boldsymbol{x}.$$

Since the POD basis functions $\boldsymbol{\phi}_i$ are divergence free and satisfy homogenized boundary conditions, the contributions coming from the pressure and the boundary terms are exactly equal to zero, with one exception. Due to the non reflecting boundary conditions (5) used in the outflow boundary, the contribution of the boundary terms in Γ_o is not exactly zero for the cylinder wake [15, for a detailed discussion]. Recently, a modal energy-flow analysis was used in [61] to elucidate the effect of the pressure term in a POD ROM of incompressible shear-flows. Essentially, they demonstrated that the effect of the pressure term is important for a mixing layer and small in a wake flow. In our approach, the pressure term is indeed omitted in the coefficients of the POD ROM. Moreover, the contribution of the boundary terms in Γ_o is supposed to be negligible. Here, neglecting these terms are numerically justified by the use of calibrated models [62, 63] where a time dependent eddy-viscosity is estimated for each POD mode [54]. With this dissipative model (see below for a justification), an accurate low order modelling of a controlled wake flow is possible (see an example in Fig. 7) and neglecting the pressure term in the linear coefficients $\mathcal{A}_i$ and the boundary terms in Γ_o have no influence.

Inserting the velocity expansion (16) into the Galerkin projection (18), some algebraic manipulations [53] leads to the reduced-order control model:

$$\begin{aligned}\frac{d\,a_i(t)}{d\,t} =& \mathcal{A}_i + \sum_{j=1}^{N_{gal}} \mathcal{B}_{ij}\, a_j(t) + \sum_{j=1}^{N_{gal}}\sum_{k=1}^{N_{gal}} \mathcal{C}_{ijk}\, a_j(t)a_k(t) \\ &+ \mathcal{D}_i\,\frac{d\,\gamma}{d\,t} + \left(\mathcal{E}_i + \sum_{j=1}^{N_{gal}} \mathcal{F}_{ij}\, a_j(t)\right)\gamma + \mathcal{G}_i\gamma^2 \qquad i = 1, \cdots, N_{gal}.\end{aligned} \tag{19}$$

The coefficients $\mathcal{A}_i$, $\mathcal{B}_{ij}$, $\mathcal{C}_{ijk}$, $\mathcal{D}_i$, $\mathcal{E}_i$, $\mathcal{F}_{ij}$ and $\mathcal{G}_i$ depend explicitly on $\boldsymbol{\phi}$, $\boldsymbol{u}_m$ and $\boldsymbol{u}_c$. Their expressions are given in Appendix A.

The POD ROM (19) is then integrated in time with a fourth order Runge-Kutta scheme from a given set of initial conditions

$$a_i(0) = (\boldsymbol{u}(\boldsymbol{x},\,0) - \boldsymbol{u}_m(\boldsymbol{x}) - \gamma(t)\,\boldsymbol{u}_c(\boldsymbol{x}),\, \boldsymbol{\phi}_i(\boldsymbol{x}))_\Omega \quad i = 1, \cdots,\, N_{gal}. \tag{20}$$

It yields to a set of predicted time histories for the mode amplitudes $a_i(t)$, which can be compared with the POD temporal eigenfunctions. However, it is now well known that when the equations (19) are integrated in time with initial

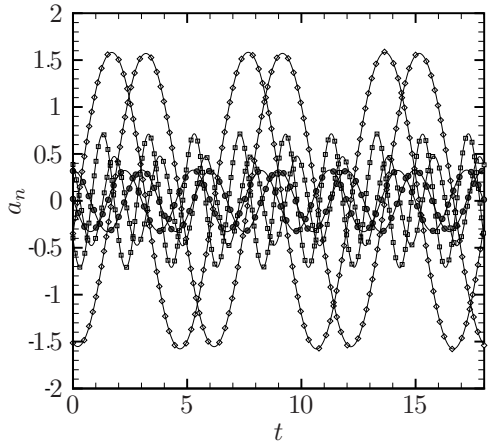

Figure 7: Comparison of the predicted (lines) and projected (symbols) mode amplitudes for the controlled cylinder ($\gamma(t) = A\sin(2\pi St_f\, t)$ with $A = 2$ and $St_f = 0.5$) at the design conditions. The system (19) is integrated in time using an eddy-viscosity model function of time and of the POD index number.

conditions obtained from corresponding direct numerical simulations, a gradual drifting from the full-state solution to another erroneous state may arise after tens vortex shedding periods, prohibiting a correct description of the long-term dynamics [64]. Even worse, in some cases, the short-term dynamics of the POD ROM may not be sufficiently accurate to be used as a surrogate model of the original high-fidelity models. Essentially, two sources of numerical errors can be identified. First, as it was already discussed, the pressure term is often neglected in the POD ROM. In many closed flows, it can be demonstrated rigorously that the contribution of the pressure term is exactly zero. For convectively unstable shear layers, as the mixing layer or the wake flow, it was proved in [61] that neglecting the pressure term may lead to large amplitude errors in the Galerkin model from where the need for introducing a pressure term representation [61, 62]. The second source of numerical errors is the truncation involved in the POD-Galerkin approach. Indeed, since only the most energetic POD modes are kept, the POD ROM is not sufficiently dissipative to prevent erroneous time amplifications of its solution. This problem is similar to that of Large Eddy Simulation where the energy transfers between the resolved scales and the subgrid scales have to be modelled [65]. Recently, Karniadakis employed the same dissipative model called Spectral Vanishing Viscosity Model (SVVM) to formulate alternative LES approaches [66] and to improve the accuracy of POD flow models [64]. Here, the POD ROM (19) is stabilized by the introduction of a time dependent eddy-viscosity model estimated for each POD mode as the solution of an auxiliary optimization problem [54, for a description]. This approach can be viewed as a calibration procedure of the POD-Galerkin system similar to the methods recently introduced in [62] for the pressure model or in [63] for the polynomial coefficients of the system.

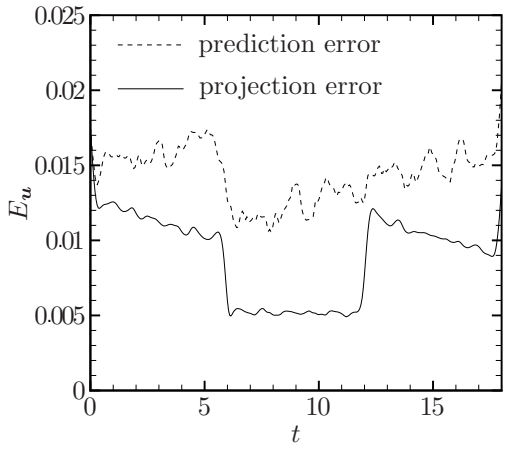

Figure 8: Comparison of the prediction and projection relative errors based on $\boldsymbol{u}$ for the controlled cylinder wake flow ($\gamma(t) = A\sin(2\pi St_f\, t)$ with $A = 2$ and $St_f = 0.5$).

As shown in Fig. 7 for a controlled flow ($\gamma(t) = A\sin(2\pi St_f\, t)$ with $A = 2$ and $St_f = 0.5$), when the POD ROM is stabilized numerically, excellent qualitative and quantitative agreements are found between the integrated time histories of the POD modes kept in the truncation (predicted modes) and the results obtained by the direct numerical simulation (projected modes). The ability of the POD ROM to predict correctly the dynamics of the controlled flow is further assessed by the time evolution of the relative error based on $\boldsymbol{u}$, $E_{\boldsymbol{u}}$. This error measure is defined as:

$$E^2_{\boldsymbol{u}}(t) = \frac{\left(\boldsymbol{u} - \widehat{\boldsymbol{u}}^{[m,c,1,\cdots,N_{gal}]}, \boldsymbol{u} - \widehat{\boldsymbol{u}}^{[m,c,1,\cdots,N_{gal}]}\right)_\Omega}{(\boldsymbol{u},\boldsymbol{u})_\Omega},$$

where $\widehat{\boldsymbol{u}}^{[m,c,1,\cdots,N_{gal}]}$ corresponds to the approximation of the exact flow $\boldsymbol{u}$ when only the first N_{gal} POD modes are retained in (16). Figure 8 represents a comparison of the corresponding error measures for the predicted modes (prediction error) and the projected modes (projection error). As it could be expected according to the optimality of the POD basis functions, the values of the projection error remain low throughout the time window. In addition, even if the prediction error is slightly higher than the projection error, no time amplification of the errors is observed. Consequently, the POD ROM (19), developed using the control function method, represents accurately, at least at the design parameters, the dynamics of a controlled wake flow. Although the range of validity of the POD ROM is not clearly determined, it can be expected that the same POD-Galerkin model is also a suitable model for other similar control parameters. However, the same reduced-order model might deliver no reliable information on the flow dynamics under a completely different control influence. Consequently, some sort of iterative technique is required, in which the construction of reduced-order models is coupled with the iteration of the optimization process. Of course, the crucial point is to decide whether or not a POD ROM

has to be adapted to a new flow dynamics. In addition, it would be highly desirable that some mathematical guarantees exist that an optimization approach based on POD ROM will converge to a solution of the original problem.

5 Optimization by Trust-Region methods and POD Reduced-Order Models

The philosophy of combining trust-region methods with approximation models of different level of reliability is a well known technique in multidisciplinary design optimization that is named surrogate optimization [44]. In the spirit of this approach, the Trust-Region Proper Orthogonal Decomposition (TRPOD) was recently proposed in [50] and [67] as a way to overcome the main difficulties related to the use of a POD ROM to solve an optimization problem. First, when the POD technique is embedded into the concept of trust-region frameworks with general model functions (see [68] for a comprehensive survey or [51] for an introduction on trust-region methods) a mechanism is provided to decide when an update of the POD ROM is necessary during the optimization process. Second, from a theoretical point of view, global convergence results exist [50] that prove that the iterates produced by the optimization algorithm, started at an arbitrary initial iterate, will converge to a local optimizer for the original model.

Hereafter, we consider that the flow control problem (minimization of the mean drag coefficient for example) can be formulated as an unconstrained optimization problem

$$\min_{\boldsymbol{c}\in\mathbb{R}^n} \mathcal{J}(\boldsymbol{\zeta}_{NS}(\boldsymbol{c}),\, \boldsymbol{c}) \tag{21}$$

where $\mathcal{J} : \mathbb{R}^m \times \mathbb{R}^n \mapsto \mathbb{R}$ represents the objective function and where $\boldsymbol{\zeta}_{NS}$ and $\boldsymbol{c}$ respectively represent the state variables obtained by numerical resolution of the state equations and the control variables. The subscript NS means that the state equations which connect the control variables $\boldsymbol{c}$ to the state variables are the Navier-Stokes equations.

Since an accurate computation of the state variables $\boldsymbol{\zeta}$ for given $\boldsymbol{c}$ is computationally expensive when the Navier-Stokes equations are used as the state equations, the evaluation of $\mathcal{J}$ during the solution of the optimization process (21) is computationally expensive. A reduction of numerical cost can be achieved by employing a POD ROM as the state equation. In such a way an approximate solution $\boldsymbol{\zeta}_{POD}$ of the state variables $\boldsymbol{\zeta}$ is obtained and the optimization problem (21) is then replaced by a succession of subproblems of the form

$$\min_{\boldsymbol{c}\in\mathbb{R}^n} \mathcal{J}(\boldsymbol{\zeta}_{POD}(\boldsymbol{c}),\, \boldsymbol{c}). \tag{22}$$

Usually, a POD ROM is constructed for a specific flow configuration, e.g., for an uncontrolled flow or for a flow altered by a specified control. Therefore, the range of validity of a given POD ROM is generally restricted to a region located in the vicinity of the design parameters in the control parameter space, the so-called *trust-region*. It is then necessary to update the POD ROM during the iterative process, the crucial point being to determine when such a reactualization must take place.

Let $\Delta^{(k)} > 0$ be the trust-region radius and $\boldsymbol{c}^{(k)}$ be the control vector obtained at an iterate k of the optimization process. To evaluate the function $\mathcal{J}(\boldsymbol{\zeta}_{NS}(\boldsymbol{c}^{(k)}), \boldsymbol{c}^{(k)})$, it is necessary to determine the state variables $\boldsymbol{\zeta}_{NS}(\boldsymbol{c}^{(k)})$. These variables are obtained by resolution of the high-fidelity model, the Navier-Stokes equations solved with $\boldsymbol{c} = \boldsymbol{c}^{(k)}$. Then, we compute snapshots that correspond to the flow dynamics forced by $\boldsymbol{c}^{(k)}$. These snapshots form the input ensemble necessary to generate a POD basis $\{\boldsymbol{\phi}_i^{(k)}\}_{i=1,\dots,N_{POD}}$. This POD basis can then be used via a Galerkin projection of the Navier-Stokes equation onto the POD eigenvectors to derive a POD ROM for $\boldsymbol{c}^{(k)}$ (see § 4). After integration in time of this POD ROM, the state variables $\boldsymbol{\zeta}_{POD}(\boldsymbol{c}^{(k)})$ are estimated, and thus the function $\mathcal{J}(\boldsymbol{\zeta}_{POD}(\boldsymbol{c}^{(k)}), \boldsymbol{c}^{(k)})$ is evaluated. Since this POD ROM can be employed for an optimization cycle, we define

$$m^{(k)}(\boldsymbol{c}^{(k)} + \boldsymbol{s}^{(k)}) = \mathcal{J}(\boldsymbol{\zeta}_{POD}(\boldsymbol{c}^{(k)} + \boldsymbol{s}^{(k)}), \boldsymbol{c}^{(k)} + \boldsymbol{s}^{(k)}), \tag{23}$$

as a model function for

$$f(\boldsymbol{c}^{(k)} + \boldsymbol{s}^{(k)}) = \mathcal{J}(\boldsymbol{\zeta}_{NS}(\boldsymbol{c}^{(k)} + \boldsymbol{s}^{(k)}), \boldsymbol{c}^{(k)} + \boldsymbol{s}^{(k)}), \tag{24}$$

on the trust-region $\|\boldsymbol{s}^{(k)}\| \leq \Delta^{(k)}$ around $\boldsymbol{c}^{(k)}$.

One is then brought to solve the corresponding trust-region subproblem defined as

$$\min_{\boldsymbol{s}\in\mathbb{R}^n} m^{(k)}(\boldsymbol{c}^{(k)} + \boldsymbol{s}), \quad \text{s.t.} \quad \|\boldsymbol{s}\| \leq \Delta^{(k)}. \tag{25}$$

Following the trust-region philosophy [68], it is not necessary to determine the exact step solution of the problem (25). It is sufficient to compute a trial step $\boldsymbol{s}^{(k)}$ that achieves only a certain amount of decrease for the model function [69]. However, due to the low computational costs involved to solve the reduced-order model, the problem (25) can be solved exactly (see the optimal control formulation described in section 7.1).

In order to estimate the quality of the presumed next control parameters $\boldsymbol{c}^{(k+1)} = \boldsymbol{c}^{(k)} + \boldsymbol{s}^{(k)}$ where $\boldsymbol{s}^{(k)}$ is the solution of (25), we compare the actual reduction in the true objective, $f(\boldsymbol{c}^{(k+1)}) - f(\boldsymbol{c}^{(k)})$, to the predicted reduction obtained with the model function $m^{(k)}(\boldsymbol{c}^{(k+1)}) - m^{(k)}(\boldsymbol{c}^{(k)})$. Essentially, it is this comparison that gives a measure for the current models prediction capability. If the trial step $\boldsymbol{s}^{(k)}$ yields to a satisfactory decrease in the original objective functional in comparison to the one obtained by the model function, the iteration is successful, the trial step $\boldsymbol{s}^{(k)}$ is accepted and the model $m^{(k)}$ is updated *i.e.* a new POD ROM is derived that incorporates the flow dynamics as altered by the new control $\boldsymbol{c}^{(k+1)}$. Furthermore, if the achieved decrease in f indicates a good behavior of the model $m^{(k)}$, the trust-region radius $\Delta^{(k)}$ can be increased. Now, if there is a limited predicted decrease compared to the actual decrease, we have the possibility to decrease slightly the value of the trust-region radius. For unsuccessful iterations, the trial step $\boldsymbol{s}^{(k)}$ is not accepted, the trust-region radius $\Delta^{(k)}$ is decreased and the trust-region subproblem (25) is solved again within a smaller trust-region. With the contraction of the trust-region it is more likely to have a good approximation to the true objective functional with the POD ROM. The corresponding TRPOD algorithm is schematically described in Fig. 9 and given in Appendix B. The proofs of global convergence of this algorithm are detailed in [50]. The main results can be found in [54].

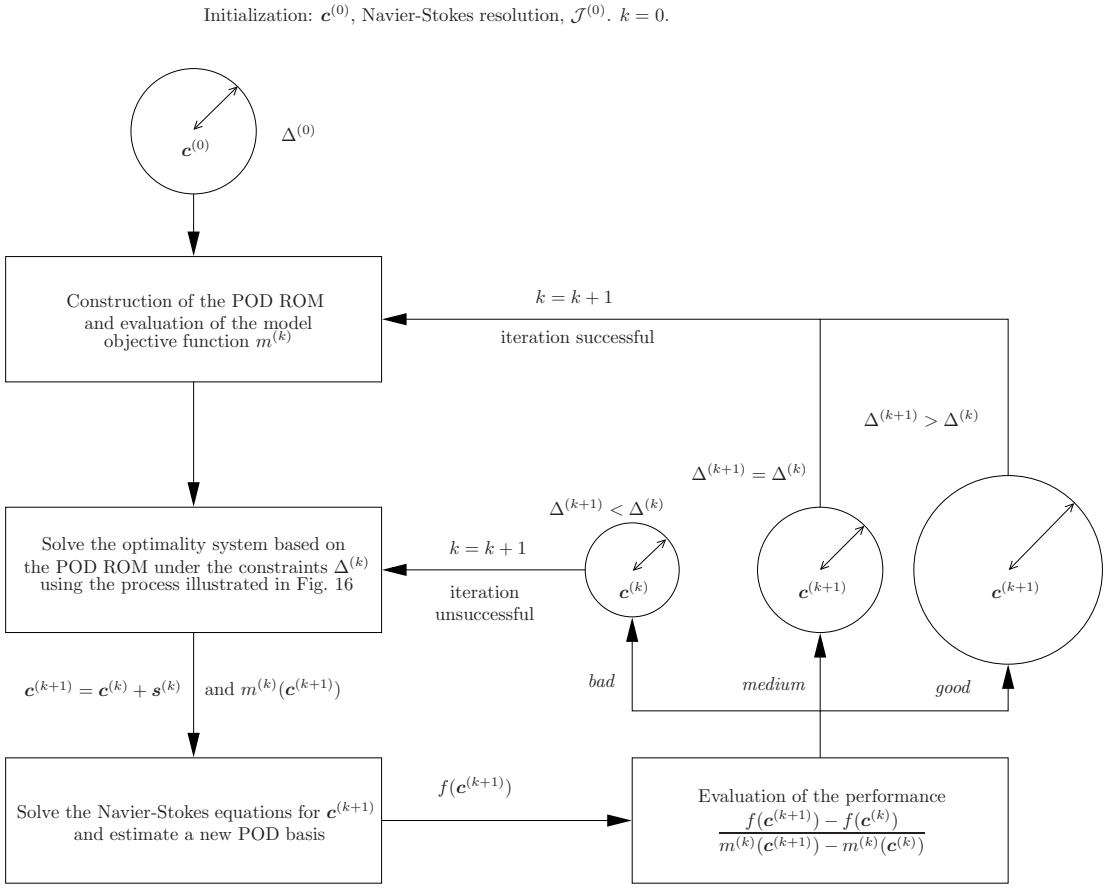

Figure 9: Schematic representation of the TRPOD algorithm.

6 A robust POD-based estimator for drag function

The objective of this study is the minimization of the mean drag coefficient of the circular cylinder estimated over a finite horizon T (see Eq. 8 for a mathematical description of this cost function). For a wake flow configuration, the instantaneous drag coefficient simply writes:

$$C_D(u,\,p) = \int_0^{2\pi} 2\,p\,n_x\,R\,d\theta - \int_0^{2\pi} \frac{2}{Re}\left(\frac{\partial u}{\partial x}\,n_x + \frac{\partial u}{\partial y}\,n_y\right)\,R\,d\theta. \tag{26}$$

Here, the state variables u and p are solutions of the high-fidelity model *i.e* the Navier-Stokes equations (1). However, the drag coefficient could be also evaluated starting from the state variables $\widehat{u}$ and $\widehat{p}$ rebuilt after integration of a POD based control model similar to (19). In this case, (26) is replaced with:

$$C_D(\widehat{u},\,\widehat{p}) = \int_0^{2\pi} 2\,\widehat{p}\,n_x\,R\,d\theta - \int_0^{2\pi} \frac{2}{Re}\left(\frac{\partial \widehat{u}}{\partial x}\,n_x + \frac{\partial \widehat{u}}{\partial y}\,n_y\right)\,R\,d\theta. \tag{27}$$

Consequently, while the real objective function writes

$$\mathcal{J}(u,\, p) = \langle C_D \rangle_T = \frac{1}{T}\int_0^T C_D(u,\, p)\, dt\,, \tag{28}$$

the model function is

$$\mathcal{J}(\widehat{u},\, \widehat{p}) = \frac{1}{T}\int_0^T C_D(\widehat{u},\, \widehat{p})\, dt. \tag{29}$$

Clearly, the pressure field appears in Eq. (29). However, for a Reynolds number roughly equal to 200, it is well-known [20, 54] that the pressure term $\int_0^{2\pi} 2\,\widehat{p}\, n_x\, R\, d\theta$ contributes to approximately 80% of the total drag coefficient. So that the model function cost represents accurately the real function cost, it is thus necessary to include the pressure field in the POD model. This is the aim of the following section.

6.1 POD reconstruction of the pressure field

6.1.1 Determination of a pressure POD basis

In most of the POD applications, only the velocity field is decomposed because the pressure data is either unavailable (this is the case of the majority of experimental work) or neglected (see the discussion in section 4.2). For our application, pressure plays an important role and must be incorporated into the POD formulation. One way is to derive the pressure from the velocity field by solving a Poisson equation in the low-dimensional POD subspace [61, section 2.4]. This method, first suggested in the context of POD by [70], seems natural for an incompressible flow. However, solving a Poisson equation in the POD subspace requires the development of a specific Poisson solver. In addition, this formulation of the problem does not constitute per se a reduced-order model of dynamics. A second option is to define a state vector $\boldsymbol{U}$ as the dimensionless velocity and pressure $\boldsymbol{U}(\boldsymbol{x},\, t) = (u(\boldsymbol{x},\, t),\, v(\boldsymbol{x},\, t),\, p(\boldsymbol{x},\, t))^T = (\boldsymbol{u}(\boldsymbol{x},\, t)^T,\, p(\boldsymbol{x},\, t))^T$ and to apply to these input data the snapshots method described in section 3. Following a similar method as the one described in section 4.1 for the velocity POD modes, a POD basis $\{\phi_i^p\}_{i=1}^{N_{POD}}$ for the pressure field can be obtained. Finally, the field $\boldsymbol{U}$ is approximated by a finite Galerkin approximation $\widehat{\boldsymbol{U}}^{[m,c,1,\cdots,N_{POD}]}$,

$$\boldsymbol{U}(\boldsymbol{x},\, t) \simeq \widehat{\boldsymbol{U}}^{[m,c,1,\cdots,N_{POD}]}(\boldsymbol{x},\, t) = \boldsymbol{U}_m(\boldsymbol{x}) + \gamma(\boldsymbol{c},\, t)\, \boldsymbol{U}_c(\boldsymbol{x}) + \sum_{i=1}^{N_{POD}} a_i(t)\, \boldsymbol{\phi}_i(\boldsymbol{x}) \tag{30}$$

where the mean field $\boldsymbol{U}_m$, the actuation mode $\boldsymbol{U}_c$ and the POD basis functions $\{\boldsymbol{\phi}_i = (\phi_i^u,\, \phi_i^v,\, \phi_i^p)^T\}_{i=1}^{N_{POD}}$ are computed using the following algorithm:

1. Determine a reference flow field $\boldsymbol{U}_c(\boldsymbol{x}) = (u_c(\boldsymbol{x}),\, v_c(\boldsymbol{x}),\, p_c(\boldsymbol{x}))^T$ as the solution of the Navier-Stokes equations for a unit control ($\gamma = 1$) and homogeneous boundary conditions for the uncontrolled boundaries.

2. Compute the mean flow $\boldsymbol{U}_m(\boldsymbol{x})$ as the ensemble average of the modified snapshots set $\{\boldsymbol{U}(\boldsymbol{x},\, t_i) - \gamma(\boldsymbol{c},\, t_i)\boldsymbol{U}_c(\boldsymbol{x})\}_{i=1}^{N_t}$:

$$\boldsymbol{U}_m(\boldsymbol{x}) = \frac{1}{N_t}\sum_{i=1}^{N_t} \{\boldsymbol{U}(\boldsymbol{x},\, t_i) - \gamma(\boldsymbol{c},\, t_i)\boldsymbol{U}_c(\boldsymbol{x})\}\,.$$

and define the fluctuation fields $\boldsymbol{U}_{snap}$:

$$\boldsymbol{U}_{snap}(\boldsymbol{x},\, t_i) = \boldsymbol{U}(\boldsymbol{x},\, t_i) - \gamma(\boldsymbol{c},\, t_i)\boldsymbol{U}_c(\boldsymbol{x}) - \boldsymbol{U}_m(\boldsymbol{x}).$$

3. Build the temporal correlation matrix C of components c_{ij} defined as:

$$c_{ij} = (\boldsymbol{U}_{snap}(\boldsymbol{x},\, t_i), \boldsymbol{U}_{snap}(\boldsymbol{x},\, t_j))_\Omega = \int_\Omega \boldsymbol{U}_{snap}(\boldsymbol{x},\, t_i) \cdot \boldsymbol{U}_{snap}(\boldsymbol{x},\, t_j)\, d\boldsymbol{x}.$$

4. Compute the eigenvalues $\lambda_1, \cdots, \lambda_{N_t}$ and the temporal eigenvectors $\boldsymbol{\Psi}_1, \cdots, \boldsymbol{\Psi}_{N_t}$ of C where $\boldsymbol{\Psi}_j = (\Psi_j(t_1), \Psi_j(t_2), \cdots, \Psi_j(t_{N_t}))^T$.

5. Compute the spatial POD basis functions $\boldsymbol{\phi}_i = (\phi_i^u,\, \phi_i^v,\, \phi_i^p)^T$ by linear combination of the temporal eigenvectors $\boldsymbol{\Psi}_i$ and the snapshots $\boldsymbol{U}_{snap}$:

$$\boldsymbol{\phi}_i(\boldsymbol{x}) = \sum_{j=1}^{N_t} \Psi_i(t_j)\, \boldsymbol{U}_{snap}(\boldsymbol{x},\, t_j).$$

6. Normalize the modes:

$$\boldsymbol{\phi}_i = \frac{\boldsymbol{\phi}_i}{\|\boldsymbol{\phi}_i\|_\Omega}.$$

As illustration of this procedure, a POD basis including the pressure field was computed from numerical snapshots of the controlled wake flow ($\gamma(t) = A\sin(2\pi St_f\, t)$ with $A = 2$ and $St_f = 0.5$). In a way identical to the velocity POD modes found previously (§ 4.2), 14 POD modes are necessary to represent 99% of the Relative Information Content. The norm of the first six pressure modes are displayed in Fig 10.

6.1.2 Accuracy of the pressure POD model

As it was previously done in section 4.2 for the velocity field, the ability of the POD pressure modes to represent correctly the dynamics of the pressure field can be assessed by the time evolution of the truncation error based on p, E_p, given by:

$$E_p^2(t) = \frac{\left(p - \widehat{p}^{[m,c,1,\cdots,N_{gal}]}, p - \widehat{p}^{[m,c,1,\cdots,N_{gal}]}\right)_\Omega}{(p,p)_\Omega},$$

where p represents the numerical exact pressure field and $\widehat{p}^{[m,c,1,\cdots,N_{gal}]}$ its POD approximation given by the expansion:

$$\widehat{p}^{[m,c,1,\cdots,N_{gal}]}(\boldsymbol{x},\, t) = p_m(\boldsymbol{x}) + \gamma(\boldsymbol{c},\, t)\, p_c(\boldsymbol{x}) + \sum_{i=1}^{N_{gal}} a_i(t)\, \phi_i^p(\boldsymbol{x}). \qquad (31)$$

For a given control $\boldsymbol{c}$, this approximation can be evaluated either using the projection coefficients, or using the prediction coefficients obtained by numerical integration of the controlled POD ROM based on $\boldsymbol{U}$. Figure 11 represents a comparison of the corresponding error measures for the projected modes (projection error) and the predicted modes (prediction error). In a way similar to what had been obtained previously for the velocity $\boldsymbol{u}$ (see Fig. 8), the projection

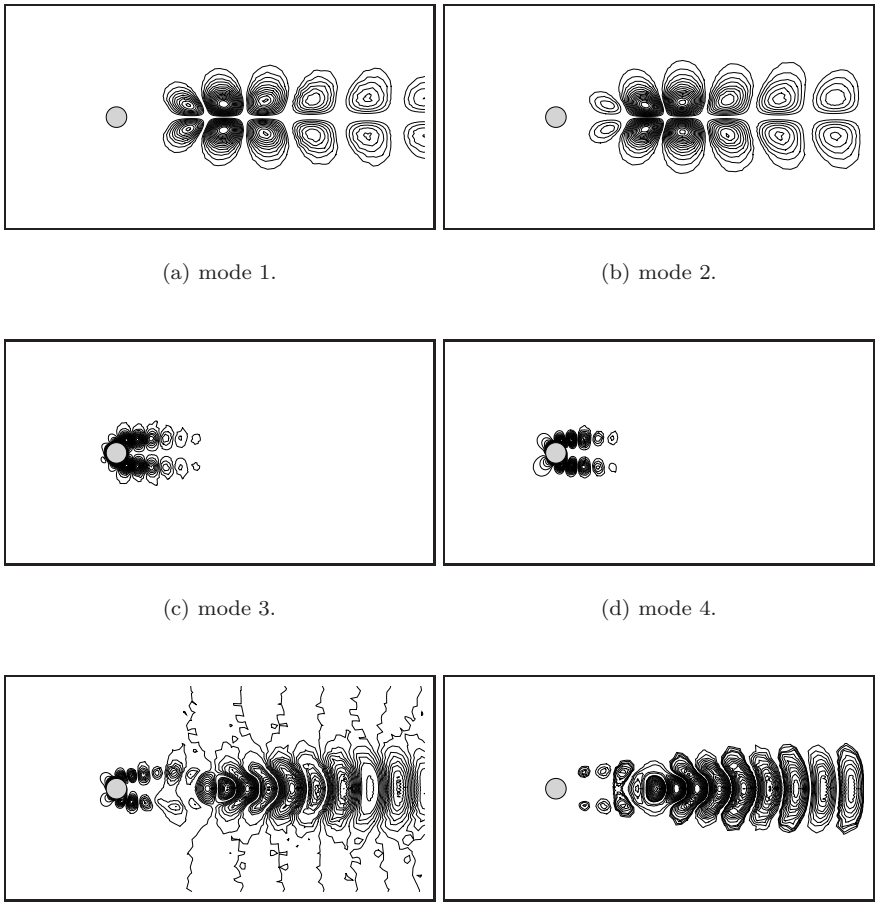

(a) mode 1. (b) mode 2.

(c) mode 3. (d) mode 4.

(e) mode 5. (f) mode 6.

Figure 10: Pressure POD basis functions for the controlled cylinder wake at $Re = 200$. The first six POD modes ϕ_n^p are visualized by iso-contour lines of their norm ($\|\phi_n^p\|_\Omega$) for $\gamma(t) = A\sin(2\pi St_f t)$ with $A = 2$ and $St_f = 0.5$.

error remains low throughout the time window, its amplitude being even lower[6] than that for the velocity field. Therefore, as it could be expected from the optimality of the POD modes, the pressure basis functions are well adapted to an accurate low-order representation of the pressure field. As for the prediction error, its values are slightly higher than those obtained for the projection error but no time amplification of the errors is observed. Consequently, one can consider that the controlled POD ROM based on $\boldsymbol{U}$ represents accurately the temporal dynamics of the velocity and pressure fields, at least for values of the control $\boldsymbol{c}$ close to those used for the design. However, although the range of the POD ROM cannot be evaluated precisely, it is well-known that the perfor-

[6]This result should however be moderated because the error made on the representation of the velocity field $\boldsymbol{u}$ is the sum of the errors on the components u and v.

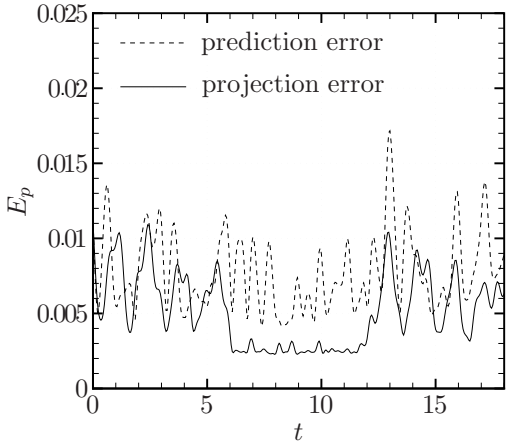

Figure 11: Comparison of the prediction and projection relative errors based on p for the controlled cylinder wake flow ($\gamma(t) = A\sin(2\pi St_f\, t)$ with $A = 2$ and $St_f = 0.5$).

mances of the model tend to deteriorate quickly with the change of the control parameters [71, 13]. Recently, Noack *et al.* [14] reviewed the key enablers to the use of empirical Galerkin models for feedback flow control and suggested the introduction of non-equilibrium modes in the POD expansion as a way to enhance the range of validity of the controlled POD ROM.

6.2 POD basis functions with non-equilibrium modes

Following [14], the minimum requirements for a POD ROM to be suitable for control design are its ability to represent at least (see Fig. 12):

1. the natural flow (dynamics I), considered as the initial condition or uncontrolled configuration,
2. the actuated flow (dynamics II), not far from the optimal controlled flow,
3. the natural transition from dynamics I to dynamics II and the forced transition from dynamics II to dynamics I.

To describe two or more operating conditions in a single POD expansion, Noack *et al.* [13, 14] proposed to add special modes, called non-equilibrium modes, to the original POD basis functions. Essentially, these non-equilibrium modes will be, either particular modes not taken into account in the original model but known to play a major role in the description of the flow dynamics (stability eigenmodes for example), or translation modes (also called shift modes) that allow the description of the transition from dynamics I to dynamics II (mode $\boldsymbol{\phi}_{neq}^{I\to II} = \boldsymbol{\phi}_0^{II} - \boldsymbol{\phi}_0^{I}$ in Fig. 12 for example). Orthonormality of the POD basis functions is then enforced in the enlarged set of modes using a Gram-Schmidt procedure described in Appendix C. Noack *et al.* [13] demonstrated that the inclusion of a shift mode representing the mean field correction

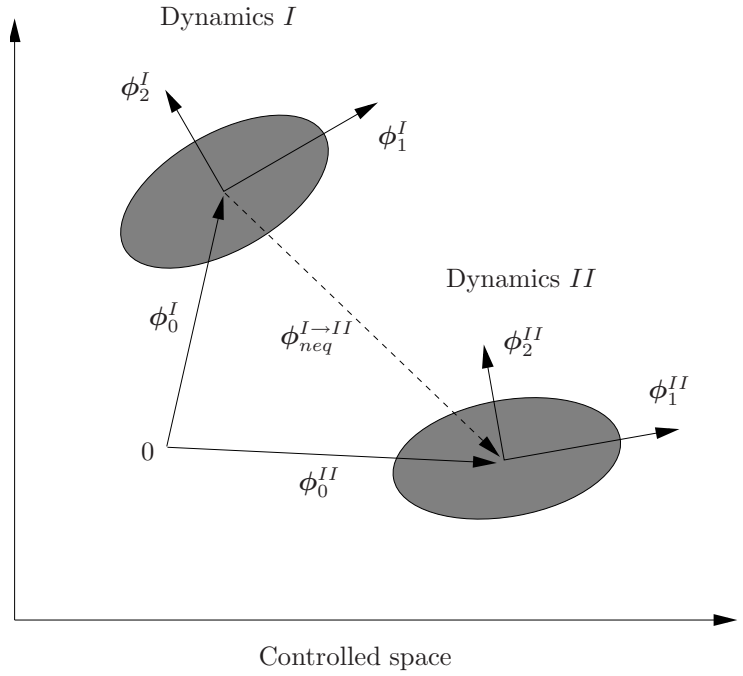

Figure 12: Schematic representation of a dynamical transition with a non-equilibrium mode (figure taken from [14]). For reasons of clarity, the physical space is reduced to three directions: one direction for the mean flow and two directions for the fluctuations.

in an empirical Galerkin model of a wake flow significantly improves the resolution of the transient dynamics from the onset of vortex shedding to the periodic von Kármán vortex street. In the same paper, it was demonstrated that the inclusion of stability eigenmodes further enhances the accuracy of fluctuation dynamics.

The velocity and pressure fields $\boldsymbol{U}$ can then be expanded as

$$\begin{aligned}\boldsymbol{U}(\boldsymbol{x},\,t) &\simeq \widehat{\boldsymbol{U}}^{[c,0,\cdots,N_{gal}+N_{neq}]}(\boldsymbol{x},\,t)\\ &= \underbrace{\sum_{i=0}^{N_{gal}} a_i(t)\,\boldsymbol{\phi}_i(\boldsymbol{x})}_{\text{Galerkin modes}} + \underbrace{\sum_{i=N_{gal}+1}^{N_{gal}+N_{neq}} a_i(t)\,\boldsymbol{\phi}_i(\boldsymbol{x})}_{\text{non-equilibrium modes}} + \underbrace{\gamma(\boldsymbol{c},\,t)\,\boldsymbol{U}_c(\boldsymbol{x})}_{\text{control function}}\quad, \quad (32)\end{aligned}$$

where $(N_{gal}+1)$ POD modes are used to represent the dynamics of the reference operating condition, N_{neq} non-equilibrium modes are added to describe new operating conditions and where the control function method is used to introduce in the model the effect of the control. For an uncontrolled flow, the mode $i=0$ is typically identified with the mean flow field $\boldsymbol{U}_m$ [72, for example]. This mode is then usually not solved in the POD ROM because its amplitude is approximately constant in time (nearly equal to 1). However, when non-equilibrium modes are introduced in the model to represent the dynamics of controlled configurations, the mean flow mode can have a transient state during

Table 2: Description of the physical and dynamical aspects of the modes appearing in expansion (32). A similar table can be found in [14].

Physical aspects	**Modes**	**Dynamical aspects**
actuation mode	$\boldsymbol{U}_c$	predetermined dynamics
mean flow mode	$\boldsymbol{U}_m$, $i=0$	$a_0 = 1$
POD modes correspond to the dynamics of the reference flow	$i=1$	**POD Reduced-Order Model** Temporal dynamics of the modes determined by integration of the POD ROM (eventually, the mode $i=0$ is solved then $a_0 \equiv a_0(t)$)
	$i=2$	
	$\cdots$	
	$i=N_{gal}$	
non-equilibrium modes correspond to the inclusion of new operating conditions	$i=N_{gal}+1$	
	$\cdots$	
	$i=N_{gal}+N_{neq}$	

which energy is exchanged with the non-equilibrium modes. Finally, the actuation mode $\boldsymbol{U}_c$ is predetermined (see § 4.1) and it is thus not modified by the dynamical evolutions intervening during the control process. The role of these modes is summarized in Table 2.

Following the method described in section 4.2 for the velocity field, a Galerkin projection of the Navier-Stokes equations on the space spanned by the first $N_{gal}+N_{neq}+1$ POD modes yields[7] to:

$$\begin{aligned}\frac{d\,a_i(t)}{d\,t} = &\sum_{j=0}^{N_{gal}+N_{neq}} \mathcal{B}_{ij}\,a_j(t) + \sum_{j=0}^{N_{gal}+N_{neq}}\sum_{k=0}^{N_{gal}+N_{neq}} \mathcal{C}_{ijk}\,a_j(t)a_k(t) \\ &+ \mathcal{D}_i\,\frac{d\,\gamma}{d\,t} + \left(\mathcal{E}_i + \sum_{j=0}^{N_{gal}+N_{neq}} \mathcal{F}_{ij}\,a_j(t)\right)\gamma(\boldsymbol{c},\,t) + \mathcal{G}_i\gamma^2(\boldsymbol{c},\,t)\,,\end{aligned} \tag{33a}$$

with the following initial conditions:

$$a_i(0) = (\boldsymbol{U}(\boldsymbol{x},\,0) - \boldsymbol{U}_m(\boldsymbol{x}) - \gamma(\boldsymbol{c},\,t)\,\boldsymbol{U}_c(\boldsymbol{x}),\,\boldsymbol{\phi}_i(\boldsymbol{x}))_\Omega\,. \tag{33b}$$

As it was already discussed at length in the introduction, the principal difficulty in the use of a POD ROM to solve an optimization problem is that neither the optimal parameters, nor the optimal path in the control parameter space are known in advance. Consequently, if the dynamics I corresponding to the uncontrolled flow is naturally known, it is impossible to know in advance what are the dynamics $II, III, IV, \cdots$ which will be the most relevant to introduce in the model. Recent work [10] seems to demonstrate that centroidal Voronoi tessellations could be one method of intelligent sampling in parameter space. Here, a simpler method is adopted, the snapshots being taken randomly in the control parameter space. Hereafter, the following dynamics are considered:

[7] Here, the Galerkin projection of the Navier-Stokes equations onto the POD modes is carried out with only the velocity components of the POD modes. Rigorously, the advantage of the orthogonality property is lost. However, the errors made on the coefficients of the POD ROM (33) are low. These errors are overall taken into account with the same calibration procedure already used for the model (19). The order of magnitude of the reconstruction errors for the velocity fields is comparable with that which had been obtained in the case of the POD ROM (19) (see Fig. 8). The reconstruction error of the pressure by the model (33) is also very low (see Fig. 11).

- dynamics I: controlled flow with $A = 2$ and $St = 0.5$,
- dynamics II : controlled flow with $A = 4$ and $St = 0.1$,
- dynamics III : natural flow $A = 0$,
- dynamics IV : unstable steady basic flow. It was argued in [30] that this configuration corresponds to the lowest mean drag reduction that can be achieved under rotary control of the cylinder.

In addition, since the objective is the mean drag reduction of the wake flow, the non-equilibrium modes will correspond only to averaged flows. The main Galerkin and non-equilibrium modes used to derive the POD ROM (33) are represented on Fig. 13. Finally, after integration in time, the solutions $\{a_i\}_{i=0}^{N_{gal}+N_{neq}}$ of the model (33) can be used to approximate the drag coefficient.

6.3 Construction of the surrogate drag function

In order to simplify the future notations, one introduces the *drag operator* $\mathcal{C}_{\mathcal{D}}$ defined as:

$$\begin{aligned} \mathcal{C}_{\mathcal{D}} : \mathbb{R}^3 &\to \mathbb{R} \\ \boldsymbol{b} &\mapsto 2\int_0^{2\pi} \left(b_3 n_x - \frac{1}{Re}\frac{\partial b_1}{\partial x} n_x - \frac{1}{Re}\frac{\partial b_1}{\partial y} n_y \right) R\, d\theta \,, \end{aligned} \tag{34}$$

where $\boldsymbol{b} = (b_1,\, b_2,\, b_3)^T$ denotes any given vector in $\mathbb{R}^3$. For $\boldsymbol{U} = (u,\, v,\, p)^T$, the vector corresponding to the velocity and pressure fields obtained as solutions of the Navier-Stokes equations, $C_D(t) = \mathcal{C}_{\mathcal{D}}(\boldsymbol{U})$ where C_D represents the instantaneous drag coefficient defined in Eq. (26). If the drag operator is applied to expansion (32), a model function of the drag coefficient is obtained:

$$\widehat{C_D}(t) = \mathcal{C}_{\mathcal{D}}(\widehat{\boldsymbol{U}}^{[c,0,\cdots,N_{gal}+N_{neq}]}) = \gamma(\boldsymbol{c},\, t)\, \mathcal{C}_{\mathcal{D}}(\boldsymbol{U}_c) + \sum_{i=0}^{N_{gal}+N_{neq}} a_i(t)\, \mathcal{C}_{\mathcal{D}}(\boldsymbol{\phi}_i).$$

Since the field $\boldsymbol{U}_c$ is predetermined and have circular symmetry (see Fig.13(k) for the actuation mode $\boldsymbol{u}_c$ for example), it does not contribute to the drag coefficient and thus $\mathcal{C}_{\mathcal{D}}(\boldsymbol{U}_c) \equiv 0$. Put $N_i = \mathcal{C}_{\mathcal{D}}(\boldsymbol{\phi}_i)$, the model function becomes:

$$\widehat{C_D}(t) = \sum_{i=0}^{N_{gal}} a_i(t) N_i + \sum_{i=N_{gal}+1}^{N_{gal}+N_{neq}} a_i(t) N_i. \tag{35}$$

To highlight in this expression the relative contributions of the weakly unsteady terms and the strongly unsteady fluctuations, this model function can be rewritten:

$$\widehat{C_D}(t) = \underbrace{a_0(t)N_0 + \sum_{i=N_{gal}+1}^{N_{gal}+N_{neq}} a_i(t) N_i}_{\text{evolution of the mean drag}} + \underbrace{\sum_{i=1}^{N_{gal}} a_i(t) N_i}_{\text{fluctuations } C'_D(t)} \quad . \tag{36}$$

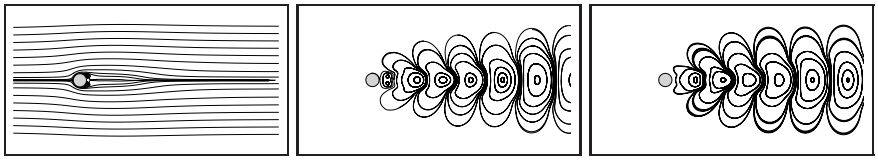

(a) Mean controlled flow I.

(b) 1st POD mode of I.

(c) 2nd POD mode of I.

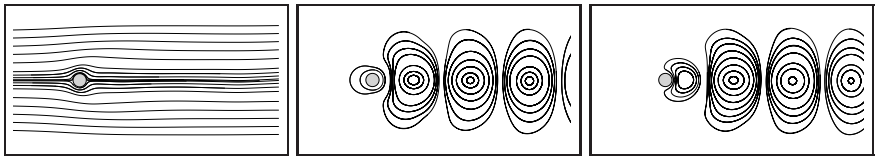

(d) Mean controlled flow II.

(e) 1st POD mode of II.

(f) 2nd POD mode of II.

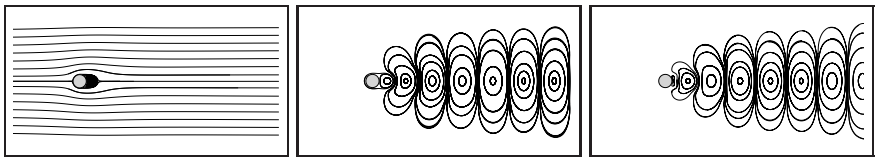

(g) Mean natural flow III.

(h) 1st POD mode of III.

(i) 2nd POD mode of III.

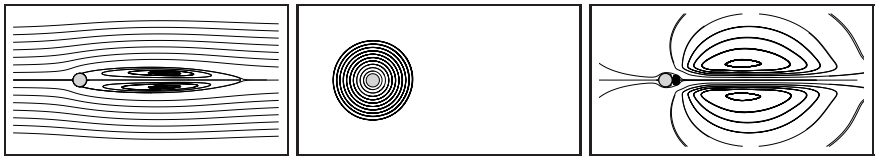

(j) Steady basic flow IV.

(k) Actuation mode $\boldsymbol{u}_c$.

(l) Shift mode from III to IV.

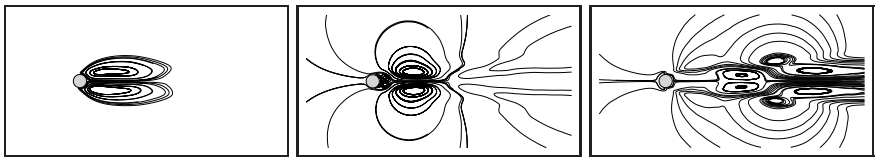

(m) Shift mode from I to II.

(n) Shift mode from I to III.

(o) Shift mode from I to IV.

Figure 13: Modes considered in the reduced-order control model (33) of the cylinder wake at $Re = 200$. In all sub-figures, the flow is visualized with streamlines.

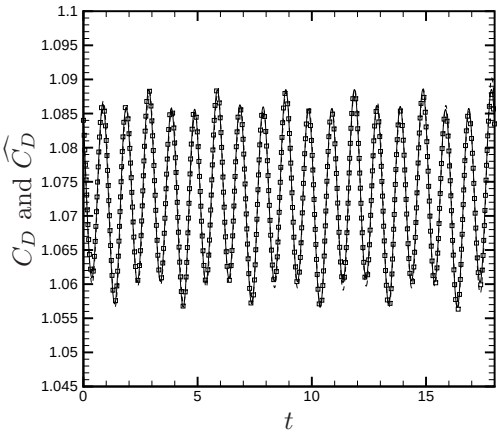

Figure 14: Comparison of the real drag coefficient C_D (symbols) and model function (lines) of the drag coefficient for the controlled cylinder wake flow ($\gamma(t) = A\sin(2\pi\, St_f\, t)$ with $A = 2$ and $St_f = 0.5$).

Finally, since the average of the fluctuations estimated over a finite time horizon T equal to a few periods of vortex shedding is approximately null, the model objective function could be written as:

$$\widehat{\mathcal{J}} = \langle \widehat{C_D}(t) \rangle_T = \frac{1}{T} \int_0^T \left(a_0(t) N_0 + \sum_{i=N_{gal}+1}^{N_{gal}+N_{neq}} a_i(t) N_i \right) dt. \tag{37}$$

The robustness of these model functions to the variations of the flow control parameters is measured by the capacity which has the POD ROM (33) to represent the variations of the real mean drag coefficient when the control law γ used for the numerical integration of the system varies. Indeed, even if the POD basis functions $\boldsymbol{\phi}_i$ employed for the Galerkin projection correspond to reference control parameters, the coefficients a_i depend implicitly on the specific control law used to solve the system (33). For example, if this system is solved with a control law γ identical to that used to derive the model then the coefficient a_0 is approximately equal to a constant and the terms $\{a_i\}_{i=N_{gal}+1}^{N_{gal}+N_{neq}}$ are all identically null. The mean field then tends towards $a_0\boldsymbol{\phi}_0$ and the value of the objective function converges towards $a_0 N_0$. On the other hand, if the system (33) is solved with a value of γ different from that used to derive the model then it is possible that the mode a_0 interacts with the non-equilibrium modes $\{a_i\}_{i=N_{gal}+1}^{N_{gal}+N_{neq}}$ leading to a variation of the mean drag coefficient.

The model function of the drag coefficient is validated once again for the controlled wake flow characterized by $A = 2$ and $St_f = 0.5$. Figure 14 displays a comparison of the real drag coefficient (26) obtained numerically for the Navier-Stokes equations and the model function of the drag coefficient (36) determined after time integration of the system (33). At the design parameters, excellent qualitative agreements are obtained not only for the mean drag coefficient but

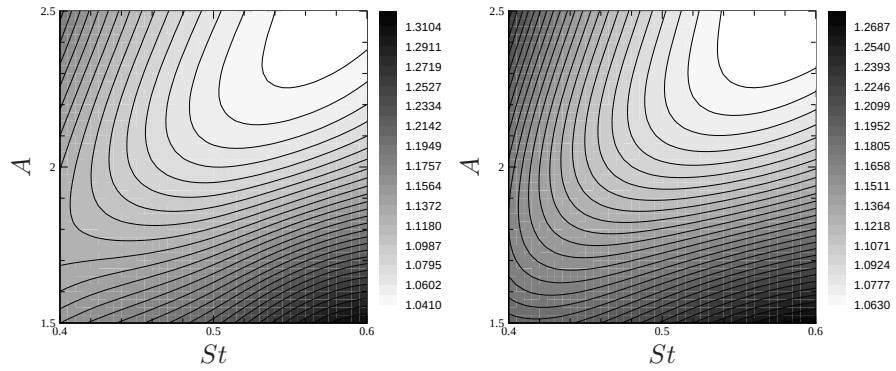

(a) Real objective function $\mathcal{J}$. (b) Model objective function $\widehat{\mathcal{J}}$.

Figure 15: Iso-values of the real and model objective functions associated to the mean drag coefficient.

also for the amplitudes and the characteristic frequencies of the oscillations. The next stage consists in checking if the model objective function (37) is suitable to represent the behavior of the real objective function (28) for control parameters A and St_f close to those corresponding to the reference flow. The dynamical system (33) is then integrated in time for various values of the control parameters located in a domain $\mathcal{D}$ centered on the reference parameters $A = 2$ and $St_f = 0.5$. For $\mathcal{D} = \{1.5 \leq A \leq 2.5 \ ; \ 0.4 \leq St \leq 0.6\}$, the iso-values of the real and model objective functions, respectively $\mathcal{J}$ and $\widehat{\mathcal{J}}$, are compared in Fig. 15. The values and the variations of these two functions are similar on the domain $\mathcal{D}$ (the maximum value of the relative error is equal to 3.9 %), thus validating the choice of the model function (37). Thereafter, this model function will thus be used to determine, using the TRPOD algorithm described in section 5, the control law that minimizes the mean drag coefficient. Finally, note that the use of POD expansions without the addition of non-equilibrium modes or a too large domain $\mathcal{D}$ can lead to erroneous results [54].

7 Drag minimization of the cylinder wake flow by POD-based adaptive controllers

Solving a flow control problem with POD reduced-order models has to face the problem that models constructed for an uncontrolled flow or a specific controlled flow are possibly unreliable models to represent the flow dynamics altered by a new control. To cope with this difficulty, we propose in this section different reduced-order adaptive procedures that improve the models by successively updating the snapshot data. Essentially, these optimization algorithms differ by the criterion which is used to decide whether or not a reduced-order model has to be adapted to a new flow configuration. In section 7.1, the optimal control approach used to solve the constrained optimization subproblem (25) is first

described. Then, the numerical results obtained with two different strategies of adaptive controllers are presented. In section 7.2.1, a suboptimal controller corresponding to a simplified version of the TRPOD algorithm is considered. Then, the optimal solutions determined with the TRPOD algorithm are presented (§ 7.2.2). Finally, the energetic efficiency of our approach is discussed and the cost reduction factors are estimated (§ 7.2.3).

7.1 Optimal control approach

The convergence behavior of trust-region methods for general model functions with inexact gradient information is usually based on a sufficient decrease condition of the objective function [68, for example]. In his original work, Fahl [50] extended these classical results and demonstrated that the exact solution of the subproblem (25) is not necessary to prove global convergence of the TRPOD algorithm. Here, because of the low computational costs of solving the POD reduced-order models, an exact optimal solution of the subproblem (25) is directly sought. For that, this subproblem is first reformulated as a constrained optimization problem which is then solved by the Lagrange multipliers method as described in [2].

Moving all the terms in the left hand side, the state equations (33) are written more simply as[8]

$$\mathcal{N}_i(\boldsymbol{a},\, \boldsymbol{c}) = 0 \qquad i = 0, \cdots, N_{gal} + N_{neq}\,, \tag{38}$$

where $\boldsymbol{a}$ is the vector containing the time-dependent expansion coefficients $\{a_i\}_{i=0}^{N_{gal}+N_{neq}}$ and $\boldsymbol{c}$ is the control vector whose components are the amplitude A and the Strouhal number St_f which define the sinusoidal control law $\gamma(t)$.

Thereafter, to simplify the various writings, the fluctuation term $C'_D(t) = \sum_{i=1}^{N_{gal}} a_i(t)N_i$ of the drag coefficient is included in (37). Therefore, the model objective function $\widehat{\mathcal{J}}$ is expressed as

$$\widehat{\mathcal{J}}(\boldsymbol{a}) = \frac{1}{T}\int_0^T J(\boldsymbol{a})\, dt\,, \tag{39}$$

where $J(\boldsymbol{a}) = \sum_{i=0}^{N_{gal}+N_{neq}} a_i(t)N_i$. In this expression, the state variables $\boldsymbol{a}$ depend implicitly of the control $\boldsymbol{c}$ used to integrate the state equations (38).

However, since we are interested by the exact minimization of the objective function $\widehat{\mathcal{J}}$ in the trust-region characterized by its radius Δ, it is useless to introduce a penalization term expressing the cost of the control as that is usually done. In the same way, the objective function $\widehat{\mathcal{J}}$ being sufficiently regular (see Fig. 5), the minimization of $\widehat{\mathcal{J}}$ in the trust-region is well-posed and it is not more necessary to introduce a Tikhonov-type regularization term as in [39].

Finally, the constrained optimization problem

$$\min_{\boldsymbol{c}} \widehat{\mathcal{J}}(\boldsymbol{a}) \quad \text{subject to} \quad \boldsymbol{\mathcal{N}}(\boldsymbol{a},\, \boldsymbol{c}) = \boldsymbol{0}\,, \tag{40}$$

[8] In order to simplify the expressions of the optimality system, we will not specify in the notations of this section that the state equations depend on the iteration number k of the TRPOD algorihtm.

is transformed to an unconstrained optimization problem by defining the Lagrangian functional

$$\mathcal{L}(\boldsymbol{a},\, \boldsymbol{c},\, \boldsymbol{\xi}) = \frac{1}{T}\int_0^T \left(J(\boldsymbol{a}) - \sum_{i=0}^{N_{gal}+N_{neq}} \xi_i\, \mathcal{N}_i(\boldsymbol{a},\, \boldsymbol{c}) \right) dt\,, \tag{41}$$

where $\boldsymbol{\xi}$ are Lagrange multipliers (also known as adjoint state variables) that enforce the state equations (38). The optimality system can be derived by taking variations of the Lagrangian with respect to the adjoint, state and control variables.

Setting the first variation of the Lagrangian with respect to the Lagrange multipliers $\boldsymbol{\xi}$ equal to zero and arguing that the variation of $\boldsymbol{\xi}$ is arbitrary in $[0, T]$, simply recovers the *state equations* (38).

Setting the first variation of $\mathcal{L}$ with respect to the state variables $\boldsymbol{a}$ to zero and arguing that the variation of $\boldsymbol{a}$ is arbitrary in $[0, T]$, and at $t = T$, yields the *adjoint equations*:

$$\frac{d\,\xi_i(t)}{dt} = -\sum_{j=0}^{N_{gal}+N_{neq}} \left(\mathcal{B}_{ji} + \gamma(\boldsymbol{c},\, t)\, \mathcal{F}_{ji} + \sum_{k=0}^{N_{gal}+N_{neq}} (\mathcal{C}_{jik} + \mathcal{C}_{jki})\, a_k(t) \right) \xi_j(t) - \frac{1}{T} N_i\,, \tag{42a}$$

and the terminal conditions:

$$\xi_i(T) = 0. \tag{42b}$$

Note that the adjoint system (42) is posed backward in time, i.e. terminal conditions are given at $t = T$ instead of initial conditions.

Defining $\mathcal{L}_i = -\frac{d\xi_i}{dt}\mathcal{D}_i + \xi_i \left(\mathcal{E}_i + \sum_{j=0}^{N_{gal}+N_{neq}} \mathcal{F}_{ij} a_j + 2\gamma(\boldsymbol{c},\, t)\mathcal{G}_i \right)$ and taking the derivative of the Lagrangian with respect to the control variables $\boldsymbol{c}$ yields the following vector equation

$$\boldsymbol{\nabla}_{\boldsymbol{c}} \widehat{\mathcal{J}} = \frac{1}{T}\int_0^T \left(\sum_{i=0}^{N_{gal}+N_{neq}} \mathcal{L}_i \right) \boldsymbol{\nabla}_{\boldsymbol{c}}\, \gamma\, dt\,, \tag{43}$$

which can be projected onto the two control directions A and St_f to get:

$$\delta\widehat{\mathcal{J}}_A = \frac{1}{T}\int_0^T \left(\sum_{i=0}^{N_{gal}+N_{neq}} \mathcal{L}_i \right) \sin(2\pi St_f\, t)\, dt\,, \tag{44a}$$

and

$$\delta\widehat{\mathcal{J}}_{St_f} = \frac{1}{T}\int_0^T 2\pi\, A\, t \left(\sum_{i=0}^{N_{gal}+N_{neq}} \mathcal{L}_i \right) \cos(2\pi St_f\, t)\, dt. \tag{44b}$$

These equations, also known as *optimality conditions*, are only equal to zero at the minimum of the objective function.

The *optimality system* formed by the state equations (33), the adjoint equations (42) and the optimality conditions (44a) and (44b) represents the first-order Karush-Kuhn-Tucker optimality conditions for the constrained optimization problem (40). This system of coupled ordinary differential equations could

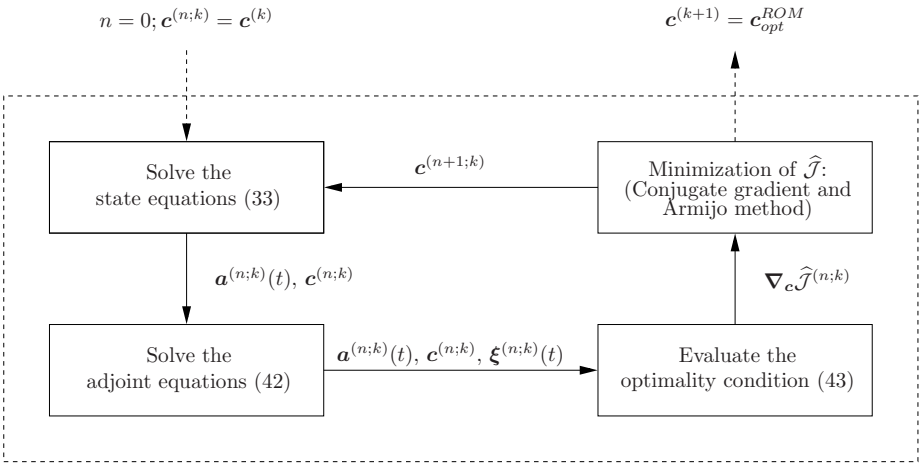

Figure 16: Solution of the reduced-order optimality system (schematic representation).

be solved directly using a "one-shot method". However, due to large storage and CPU costs, this system is usually solved using the iterative process illustrated in Fig. 16. In the present approach, a direction of descent is determined by the Fletcher-Reeves version of the Conjugate Gradient Method [41, for example]. Let k be the index of the external loop associated to the TRPOD algorithm. In every iteration n of the inner loop, the control vector is then updated according to

$$\boldsymbol{c}^{(n+1;k)} = \boldsymbol{c}^{(n;k)} + \omega^{(n;k)}\, \boldsymbol{d}^{(n;k)}, \tag{45}$$

where $\boldsymbol{d}^{(n;k)}$ represents the conjugate direction given by

$$\boldsymbol{d}^{(n;k)} = -\boldsymbol{\nabla}_{\boldsymbol{c}}\widehat{\mathcal{J}}^{(n;k)} + \beta^{(n;k)}\boldsymbol{d}^{(n-1;k)}, \qquad \boldsymbol{d}^{(0;k)} = -\boldsymbol{\nabla}_{\boldsymbol{c}}\widehat{\mathcal{J}}^{(0;k)} \tag{46}$$

with $\beta^{(n;k)}$ a coefficient given by

$$\beta^{(n;k)} = \frac{\left(\boldsymbol{\nabla}_{\boldsymbol{c}}\widehat{\mathcal{J}}^{(n;k)}, \boldsymbol{\nabla}_{\boldsymbol{c}}\widehat{\mathcal{J}}^{(n;k)}\right)}{\left(\boldsymbol{\nabla}_{\boldsymbol{c}}\widehat{\mathcal{J}}^{(n-1;k)}, \boldsymbol{\nabla}_{\boldsymbol{c}}\widehat{\mathcal{J}}^{(n-1;k)}\right)}. \tag{47}$$

The linear search parameter $\omega^{(n;k)}$ is computed at each iteration n by the backtracking Armijo method [51], an algorithm that assures that the corresponding step is not too small and verifies the Goldstein condition. The iterative method is stopped when two following values of the functional $\widehat{\mathcal{J}}$ are sufficiently close i.e. when $|\Delta\widehat{\mathcal{J}}(\boldsymbol{a})| = |\widehat{\mathcal{J}}^{(n+1;k)}(\boldsymbol{a}) - \widehat{\mathcal{J}}^{(n;k)}(\boldsymbol{a})| < 10^{-5}$.

7.2 Numerical results of two POD-based adaptive controllers

In the original version of the TRPOD approach (see algorithm B for a thorough description and Fig. 9 for a schematic representation), the radius $\Delta^{(k)}$ of the trust-region is modified, if necessary, at each iteration k by comparing the actual reduction of the true objective function $\mathcal{J}(\boldsymbol{U}(\boldsymbol{c}))$ to the predicted reduction

obtained with the model function $m = \widehat{\mathcal{J}}(\widehat{\boldsymbol{U}}(\boldsymbol{c}))$. An elementary modification of this algorithm consists in considering the radius of the trust-region constant throughout the optimization process ($\Delta^{(k+1)} = \Delta^{(k)}$) and equal to a finite or infinite given value. The results obtained for this simplified version of the TRPOD algorithm are presented in section 7.2.1. Those obtained by the TRPOD algorithm B are presented in section 7.2.2. In both cases, the stopping criterion of the adaptive procedure is $|\widehat{\mathcal{J}}^{(k)} - \widehat{\mathcal{J}}^{(k+1)}| < \varepsilon$ where the tolerance ε is arbitrarily taken equal to 10^{-5}.

As it was discussed for example in [36], a possible drawback of solving a minimization problem with a gradient-based optimization approach is that the algorithm may converge to the global minimum or to some other local minimum of the cost function depending on the relative position of the starting point to the minima. To alleviate this difficulty and evaluate the robustness of the two adaptive controllers, the optimization process will be initialized starting from several different control $\boldsymbol{c}^{(0)}$ chosen at random in the control parameter space retained for the open-loop control procedure (see Fig. 5). Hereafter, four different initial values are employed: $\boldsymbol{c}^{(0)} = (1.0\,,\,0.2)^T$, $\boldsymbol{c}^{(0)} = (1.0\,,\,1.0)^T$, $\boldsymbol{c}^{(0)} = (6.0\,,\,0.2)^T$ and $\boldsymbol{c}^{(0)} = (6.0\,,\,1.0)^T$.

7.2.1 Suboptimal adaptive controller

The adaptive procedures considered in this section are based on algorithms originally introduced in [17] and [73]. Contrary to the TRPOD algorithm where the trust-region radius is revalued at each iteration, these authors consider the radius constant throughout the process of optimization ($\Delta^{(k+1)} = \Delta^{(k)} = \Delta$) and suppose that the range of validity of the POD ROM is independent of the specific control law used to derive it *i.e.* $\Delta = \infty$. However, since the flow dynamics depends a priori strongly on the control, it is not clear that a POD ROM, derived at iteration k of the adaptive procedure, is suitable for describe the dynamics altered by the optimal control $\boldsymbol{c}^{(k+1)}$, solution of the reduced optimization problem at the next iteration. Therefore, it was suggested in [19] to modify the original algorithm while adding, in every iteration of the iterative procedure, the snapshots computed with the last optimal control input to the snapshot set used to determine the POD basis for the next iteration. The disadvantage of this procedure is that the size of the input data grows continuously with the iteration number, increasing considerably the computational costs. Hinze and Volkwein [19] successfully applied this modified algorithm to compute suboptimal controls for the cylinder wake flow at a Reynolds number equal to 100. Nevertheless, in the present case, after a few satisfying iterations, the control parameters reached erroneous values due to the divergence in the time integration of the POD ROM (33). This behavior expressed that the model (33), derived however with the control function method and POD basis functions with non-equilibrium modes, is not sufficiently robust to represent controlled dynamics located far from the different design operating conditions. It is thus necessary to restrict the range of validity of the POD ROM in the control parameter space in a way similar to what is made for the TRPOD algorithm. Various numerical values were considered for the parameters characteristic of this trust-region, the most satisfactory [54] were $\Delta_A = 0.5$ and $\Delta_{St_f} = 0.1$ for the forcing amplitude and Strouhal number respectively. Figure 17 represents for the different initial control $\boldsymbol{c}^{(0)}$, the variations of the values of the forc-

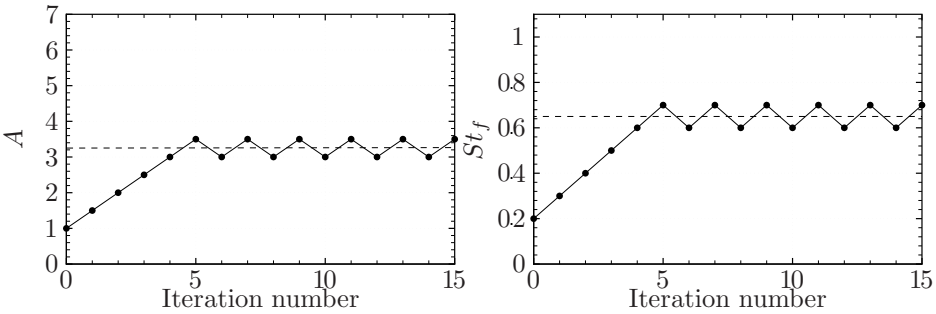

(a) $\boldsymbol{c}^{(0)} = (1.0\,,\,0.2)^T$.

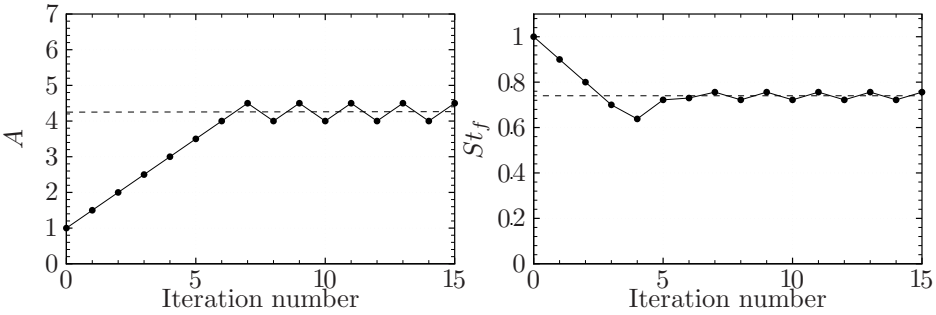

(b) $\boldsymbol{c}^{(0)} = (1.0\,,\,1.0)^T$.

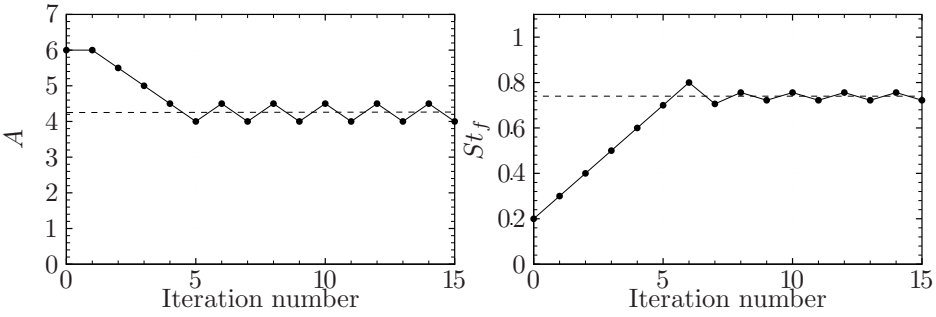

(c) $\boldsymbol{c}^{(0)} = (6.0\,,\,0.2)^T$.

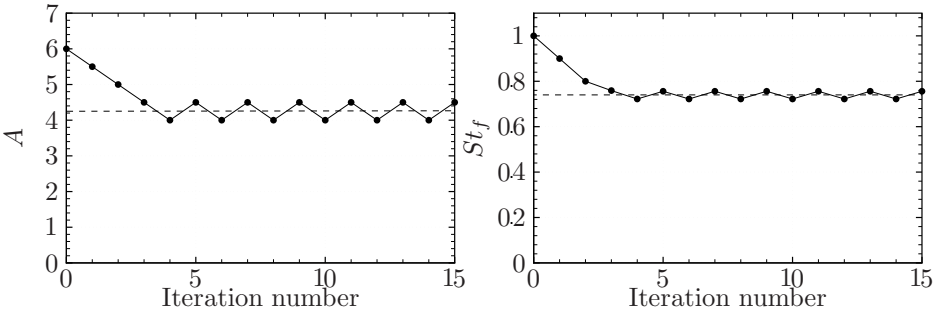

(d) $\boldsymbol{c}^{(0)} = (6.0\,,\,1.0)^T$.

Figure 17: Variations of the forcing amplitude (left) and Strouhal number (right) with respect to the iteration number. Results obtained with the adaptive method for $\Delta_A = 0.5$ and Δ_{St_f}=0.1.

ing amplitude and Strouhal number with respect to the iteration number. For $\boldsymbol{c}^{(0)} = (1.0\,,\,0.2)^T$, the forcing amplitude and Strouhal number oscillate around the values $A = 3.25$ and $St_f = 0.65$ respectively. The corresponding mean drag coefficient is $\langle C_D \rangle_T = 1.009$. For all the other values of initial parameters of control, the forcing amplitude and Strouhal number oscillate around $A = 4.25$ and $St_f = 0.74$ respectively. In this case the value of the mean drag coefficient is $\langle C_D \rangle_T = 0.993$. For the three last initial conditions, it is remarkable that the control parameters obtained by the adaptive procedure tend towards those given by numerical experimentation (see section 2.3). However, as one can note it on figure 17, the iterative process does not converge. Indeed, in the majority of the cases, the forcing amplitude oscillates constantly between the lower and the upper limits of the trust-region defined by $\Delta_A = 0.5$. Since the global minimum of the mean drag coefficient is located in a very smooth valley (see Fig. 5), it is delicate to build a model function able to predict accurately the variations of the objective function in this area. The size of the trust-region Δ is then possibly too large at some iterations. It is thus necessary to envisage a mechanism of reduction of Δ during the optimization process in order to improve the robustness of the model functions. That is precisely the interest of the trust-region methods presented in section 5.

7.2.2 Optimal adaptive controller: the TRPOD approach

According to the TRPOD algorithm B, the radius of the trust-region Δ can now be automatically either increased, or decreased during the resolution of the optimization process. Essentially, the size of the trust-region depends on the topology of the objective function. Figure 18 represents for the different initial control vector $\boldsymbol{c}^{(0)}$, the variations of the values of the forcing amplitude and Strouhal number with respect to the iteration number. When the numerical convergence of the iterative procedure is achieved, the optimal control parameters are $A = 4.25$ and $St_f = 0.738$. These values of parameters, which entirely define the optimal control law $\gamma_{opt}(t)$, are obtained in less than ten resolutions of the Navier-Stokes equations, whatever the initial condition considered (a more significant number of iterations is however represented in Fig. 18 to highlight the convergence). This convergence can be analyzed in more details while referring to [54] where the evolutions until convergence of the main parameters of the TRPOD algorithm are given. As it was expected by the global convergence properties of the TRPOD algorithm (§ 5), these optimal control parameters tend towards the values predicted by an open-loop control approach (§ 2.3), and this, whatever the initial values used for the control parameters (see Fig. 19 which represents the convergence in the control parameter space). This proves the performance and the robustness of the TRPOD algorithm. Figure 20 represents the time evolutions of the aerodynamic coefficients, for an uncontrolled flow and for the flow forced by the optimal control law $\gamma_{opt}(t)$. These results are compared to those obtained for the unstable steady basic flow. It was argued in [30] that the basic flow generates *a priori* the lowest coefficient of drag for the configuration under study. The mean drag coefficient varies from a value equal to $\langle {C_D}^{unc} \rangle_T = 1.39$ in the uncontrolled case to a value equal to $\langle {C_D}^{opt} \rangle_T = 0.99$ when the optimal control parameters are applied. The corresponding relative mean drag reduction, defined as $\left(\langle {C_D}^{unc} \rangle_T - \langle {C_D}^{opt} \rangle_T \right) / \langle {C_D}^{unc} \rangle_T$, is equal to more than 30%. The value of the

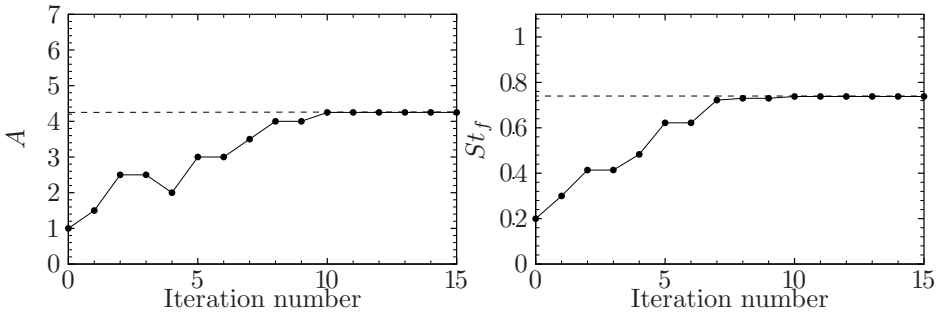

(a) $\boldsymbol{c}^{(0)} = (1.0\,,\,0.2)^T$.

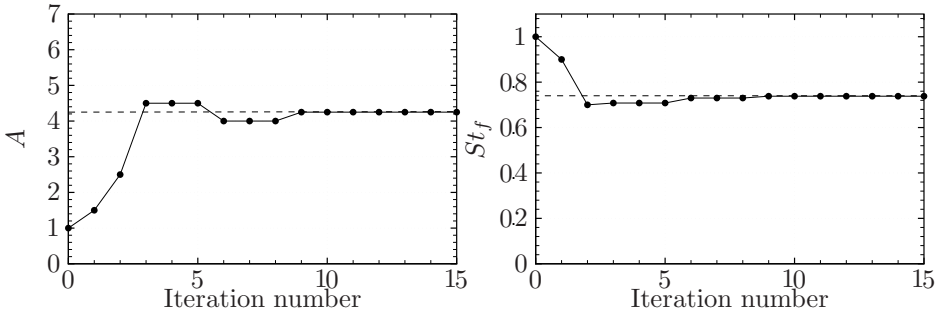

(b) $\boldsymbol{c}^{(0)} = (1.0\,,\,1.0)^T$.

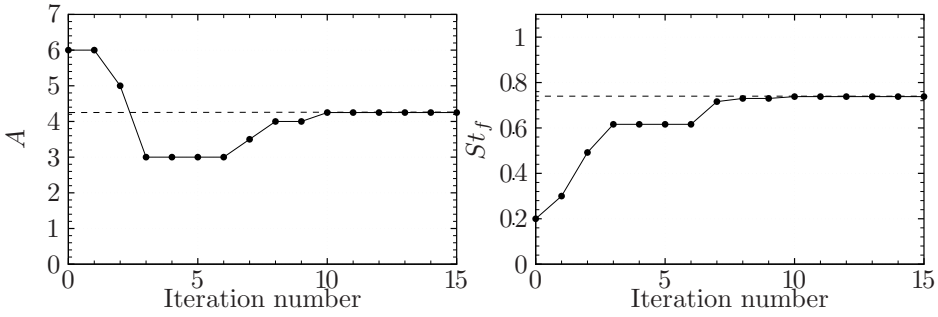

(c) $\boldsymbol{c}^{(0)} = (6.0\,,\,0.2)^T$.

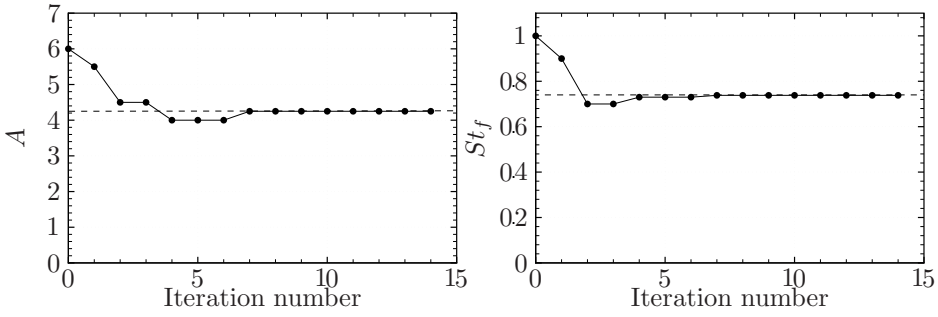

(d) $\boldsymbol{c}^{(0)} = (6.0\,,\,1.0)^T$.

Figure 18: Variations of the forcing amplitude (left) and Strouhal number (right) with respect to the iteration number. Results obtained with the TR-POD method.

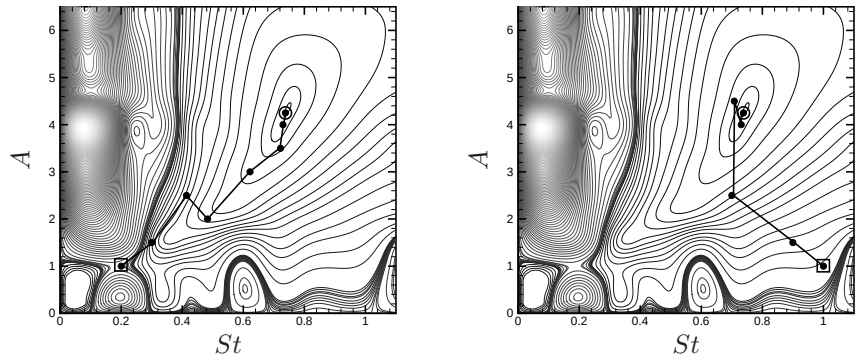

(a) $\boldsymbol{c}^{(0)} = (1.0\,,\,0.2)^T$ (b) $\boldsymbol{c}^{(0)} = (1.0\,,\,1.0)^T$

(c) $\boldsymbol{c}^{(0)} = (6.0\,,\,0.2)^T$ (d) $\boldsymbol{c}^{(0)} = (6.0\,,\,1.0)^T$

Figure 19: Evolution of the control parameters during the optimization process for the different initial values $\boldsymbol{c}^{(0)}$.

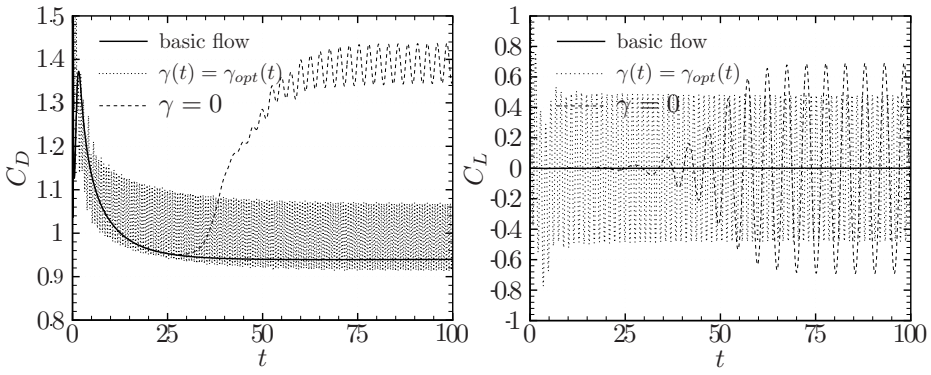

(a) Drag coefficient.

(b) Lift coefficient.

Figure 20: Time evolutions of the aerodynamic coefficients for the basic flow (solid line), uncontrolled flow ($\gamma = 0$, dashed lines) and optimally controlled flow ($\gamma(t) = \gamma_{opt}(t)$, dotted lines). Control was started at time $t = 0$.

drag coefficient for the optimally controlled flow tends towards that obtained for the unstable steady basic flow ($C_D^{basic} = 0.94$), but with a value always slightly higher. In addition, similarly to the case of the uncontrolled flow [55], the drag coefficient oscillates at a frequency equal to twice that of the lift coefficient [54]. Furthermore, the controlled flow oscillates now at the frequency of the optimal control law ($St_f = 0.738$), a phenomenon called as lock-on flow [54]. Finally, in Figs. 21(a)-21(c) we represent the vorticity fields of the uncontrolled flow, the optimally controlled flow, and the basic flow, respectively. The significant vortex-shedding phenomenon observed in Fig. 21(a) has been substantially reduced when the control is applied and the flow has been quasisymmetrized. The resulting flow approaches the symmetric state characteristic of the corresponding basic flow as can be awaited from the results of [30] and the discussion in [15]. Our results are qualitatively similar to the effects observed in [21] and [38] and confirm the arguments of [40] that the mean drag reduction is associated with control driving the mean flow toward the unstable state.

7.2.3 Discussion

The numerical results obtained here with the TRPOD algorithm agree to a large extent to results obtained in other numerical approach, where the optimal control theory is applied for the same flow configuration directly to the Navier-Stokes equations (see table 3 for the characteristics of the different algorithms).

However, quantitative comparisons of the control algorithms presented in table 3 are difficult because for the comparisons to be fair, it would be necessary that the same actuation method and the same control objectives were retained in the various studies. But the studies used for comparison were performed with either a different actuation method or a different control objective. Therefore, only qualitative comparisons of the control methodologies are possible. The reader is referred to [15] for a detailed discussion.

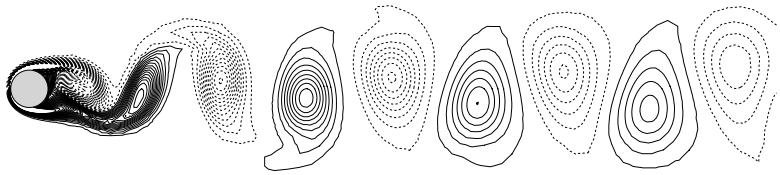

(a) Uncontrolled flow ($\gamma = 0$).

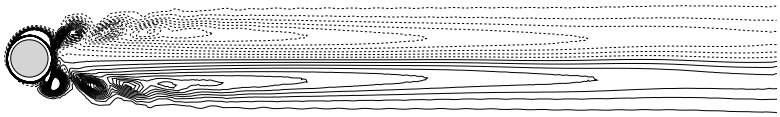

(b) Optimally controlled flow ($\gamma(t) = A\sin(2\pi St\, t)$ with $A = 4.25$ and $St = 0.738$).

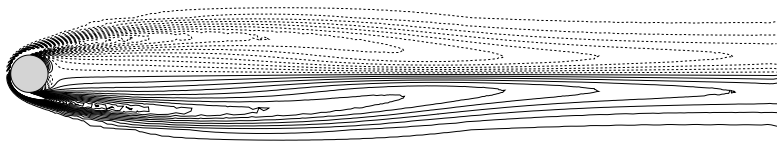

(c) Basic flow.

Figure 21: Vorticity contour plot of the wake for the uncontrolled (a), optimally controlled (b) and basic flow (c). The dashed lines correspond to negative values.

Following [40], the energetic efficiency of the control can be characterized by the Power Saving Ratio (PSR) defined as:

$$PSR = \frac{\langle P_D\rangle_T^{\text{uncontrolled}} - \langle P_D\rangle_T^{\text{controlled}}}{\langle P_C\rangle_T}\,, \tag{48}$$

where $\langle P_D\rangle_T$ and $\langle P_C\rangle_T$ represent respectively the mean of the instantaneous drag power P_D and control power P_C estimated over a finite horizon T. Except for the approach presented in [40] where the energetic efficiency is favored ($PSR \gg 1$), the different numerical studies confirmed that an harmonic rotary control is energetically inefficient without a sufficient penalization of the control input. However, our main concern in this study is not to determine the control law with the maximum energetic efficiency. Rather, our objective is

Table 3: Characteristics of the different algorithms previously used in the literature to control the laminar wake flow with an optimal control approach. The present study is included for comparison. 'Unknown' means that the value was not found in the article, an estimate is then given when it is possible. In the column entitled "State equation", 'NS' means Navier-Stokes equations and 'POD ROM' means POD Reduced-Order Model. A similar table can be found in [15].

Reference	Re	Type of optimal control law	State equation	Cost functional	Relative mean drag reduction	PSR
[38]	200	Sinusoidal $A = 3.$ $St_f = 0.75$	NS	Drag-related	30%	Unknown (certainly < 1)
[39]	100	Sinusoidal $A = 3.25$ $St_f = 1.13$	NS	Target flow ($Re = 2$)	Unknown	Unknown (certainly < 1)
[40]	150	Any	NS	Power Drag + Power Control	15%	51
[15]	200	Sinusoidal $A = 2.2$ $St_f = 0.53$	POD ROM	Drag-related	25%	0.26
Present study	200	Sinusoidal $A = 4.25$ $St = 0.738$	POD ROM	Drag	30%	0.07

to demonstrate that with an appropriate adaptive strategy, the solution of the optimization problem based on POD reduced-order models of the flow corresponds to the solution of the optimization problem based on the Navier-Stokes equations. Therefore, the most outstanding result is that the optimal control parameters obtained by the TRPOD algorithm tend towards the parameters determined in section 2.3 by an open-loop control approach, thus confirming the results of global convergence of the TRPOD.

As it can be noticed in table 3, the relative drag reduction found with the Navier-Stokes equations as state equation is the same, sometimes slightly lower, than the one found with the TRPOD algorithm, but the numerical costs (CPU and memory) associated with their control are more important. Indeed, with a gradient-based algorithm of optimization, each iteration of the optimizer requires to determine a direction of descent (resolution of an optimality system formed by the state equations, the adjoint equations and the optimality conditions) then to carry out a line search which involves the resolution of several state equations (Navier-Stokes equations or POD ROM according to the adopted approach). Let us assume that in both cases the same numerical parameters are considered to solve the equations of the optimality system, that the convergence is obtained in the same number of iteration and, finally, that the CPU time necessary to solve the adjoint equations and the optimality conditions is the same that the one used for the state equations. In this study, the CPU time necessary to obtain, with the POD ROM, the flow dynamics over a given time horizon represents 1% of the time corresponding to the resolution of the Navier-Stokes equations with the finite-element approach. Consequently, the computational time necessary to solve the optimality system based on the POD ROM can be neglected at first approximation in front of the CPU time necessary to generate the POD ROM. The computational costs related to the resolution of the optimality system based on the Navier-Stokes equations are at least ap-

proximately equal to four times that required to solve the optimization problem based on the POD ROM [54]. This cost corresponds to the case where only one optimality condition and one line search step are considered. Consequently, in practice, the reduction factor can be largely more important and that, even if additional resolutions of the Navier-Stokes equations are necessary, to evaluate the non-equilibrium modes used to build the POD basis.

With regard to memory cost, note that we need to store the state variables for all space time to solve the adjoint equations and all the adjoint variables to estimate the optimality conditions. When the finite-element simulation is used to solve the optimal control problem over a time horizon T_o, we need to store the state and adjoint variables (two velocity components and the pressure) at every time step and for each vertex of the mesh. When the POD ROM is used, we only need to store the time evolution of $\mathbf{a}$ and of the adjoint variables $\boldsymbol{\xi}$ for $N_{gal} + N_{neq} + 1$ POD modes plus the coefficients appearing in the state equation (33) *i.e.* four linear coefficients ($\mathcal{A}$, $\mathcal{D}$, $\mathcal{E}$ and $\mathcal{G}$), two quadratic coefficients ($\mathcal{B}$ and $\mathcal{F}$) and one cubic coefficient ($\mathcal{C}$). As illustration, we consider that the parameters used to solve the optimization problem are $T_o = 20$ for the time horizon, $\Delta t = 0.01$ for the optimization time-step, $N_v = 12,000$ for the number of vertices and $N_{gal} + N_{neq} + 1 = 20$ for the number of POD modes kept in the ROM where $N_{gal} = 14$ corresponds in this case to 99.9% of the Relative Information Content. After estimate (see Appendix D) we found that the memory cost of the POD ROM approach is approximately 1600 times lesser than for the Navier-Stokes model (approximately 180 if we decide to store the POD eigenfunctions to reconstruct later the velocity and pressure fields). The reduction of the numerical costs offered by our approach is so important that the study of three-dimensional unsteady complex flows by the optimal control theory becomes possible. The cost-reduction factors are comparable to the results previously found in [15] but, in this case, the global convergence of the TRPOD algorithm can be used to prove mathematically that the iterations produced by the otptimization algorithm will converge to a local optimizer for the high-fidelity model.

8 Conclusions

The objective of this paper was to illustrate the interest of combining trust-region methods and POD Reduced-Order Models to solve an optimal control problem for fluid flows. The Trust-Region POD algorithm originally introduced in [50] was used to minimize the total mean drag coefficient of a circular cylinder wake flow in the laminar regime ($Re = 200$). Since the cost functional is the mean drag, the POD basis functions were extended to the pressure data. A particular care was taken to derive a POD ROM for the pressure and velocity fields with an appropriate balance between model accuracy and robustness. The key enablers are the calibration of the POD ROM by the introduction of an optimal eddy-viscosity for each POD mode and the addition in the POD expansion of several non-equilibrium modes to describe various operating conditions. Finally, the optimal control parameters obtained with the TRPOD algorithm are $A = 4.25$ and $St_f = 0.738$. The relative mean drag reduction is equal to 30%: the mean drag coefficient varies from a value equal to 1.39 in the uncontrolled case to a value equal to 0.992 when the optimal control

parameters are applied. However, we demonstrated that this control law is energetically inefficient. These numerical results agree to a large extent to those obtained previously by other researchers [38, 40, 74] using the two-dimensional Navier-Stokes equations to solve the optimal control problem. Compared with those studies, the main advantage of our approach is that it leads to a significant reduction of the numerical costs because the optimization process itself is completely based on reduced-order models only. Indeed, when the state equations of the optimality system are POD ROMs instead of the Navier-Stokes equations, a cost reduction factor of 1600 is obtained for the memory and the optimization problem is solved approximately 4 times more quickly. Now, if we compare to our preceding study [15], where a POD ROM was coupled to an optimal control approach without any strategy for updating the reduced-order model during the optimization process, the cost reduction factors, found here, are lower. However, in this study, the use of the TRPOD algorithm mathematically proves that the solutions converge at least to a local optimum for the original high-fidelity problem, and less than ten resolutions of the Navier-Stokes equations are necessary. Due to the low computational costs involved in the optimization process and the mathematical proofs of global convergence, the TRPOD algorithm is a promising method of optimization in flow control. This approach that can easily be adapted to other configurations, should finally lead to the current resolution of unsteady, three-dimensional optimization problems for turbulent flows around complex geometries.

Acknowledgements

The authors acknowledge M. Braza (Institut de Mécanique des Fluides de Toulouse) and D. Ruiz (ENSEEIHT), who kindly provided an original version of their Matlab Navier-Stokes solver. Stimulating and fruitful discussions with Jean-Pierre Brancher and the low-dimensional modelling and control team at the Technische Universität Berlin, in particular Bernd R. Noack, are acknowledged.

A POD ROM coefficients

$$\mathcal{A}_i = -\left(\boldsymbol{\phi}_i,\, (\boldsymbol{u}_m\cdot\boldsymbol{\nabla})\boldsymbol{u}_m\right)_\Omega - \frac{1}{Re}\left((\boldsymbol{\nabla}\otimes\boldsymbol{\phi}_i)^T,\, \boldsymbol{\nabla}\otimes\boldsymbol{u}_m\right)_\Omega + \frac{1}{Re}\left[(\boldsymbol{\nabla}\otimes\boldsymbol{u}_m)\boldsymbol{\phi}_i\right]_\Gamma,$$

$$\mathcal{B}_{ij} = -\left(\boldsymbol{\phi}_i,\, (\boldsymbol{u}_m\cdot\boldsymbol{\nabla})\boldsymbol{\phi}_j\right)_\Omega - \left(\boldsymbol{\phi}_i,\, (\boldsymbol{\phi}_j\cdot\boldsymbol{\nabla})\boldsymbol{u}_m\right)_\Omega - \frac{1}{Re}\left((\boldsymbol{\nabla}\otimes\boldsymbol{\phi}_i)^T,\, \boldsymbol{\nabla}\otimes\boldsymbol{\phi}_j\right)_\Omega + \frac{1}{Re}\left[(\boldsymbol{\nabla}\otimes\boldsymbol{\phi}_j)\boldsymbol{\phi}_i\right]_\Gamma,$$

$$\mathcal{C}_{ijk} = -\left(\boldsymbol{\phi}_i,\, (\boldsymbol{\phi}_j\cdot\boldsymbol{\nabla})\boldsymbol{\phi}_k\right)_\Omega,$$

$$\mathcal{D}_i = -\left(\boldsymbol{\phi}_i,\, \boldsymbol{u}_c\right)_\Omega,$$

$$\mathcal{E}_i = -\left(\boldsymbol{\phi}_i,\, (\boldsymbol{u}_c\cdot\boldsymbol{\nabla})\boldsymbol{u}_m\right)_\Omega - \left(\boldsymbol{\phi}_i,\, (\boldsymbol{u}_m\cdot\boldsymbol{\nabla})\boldsymbol{u}_c\right)_\Omega - \frac{1}{Re}\left((\boldsymbol{\nabla}\otimes\boldsymbol{\phi}_i)^T,\, \boldsymbol{\nabla}\otimes\boldsymbol{u}_c\right)_\Omega + \frac{1}{Re}\left[(\boldsymbol{\nabla}\otimes\boldsymbol{u}_c)\boldsymbol{\phi}_i\right]_\Gamma,$$

$$\mathcal{F}_{ij} = -\left(\boldsymbol{\phi}_i,\, (\boldsymbol{\phi}_j\cdot\boldsymbol{\nabla})\boldsymbol{u}_c\right)_\Omega - \left(\boldsymbol{\phi}_i,\, (\boldsymbol{u}_c\cdot\boldsymbol{\nabla})\boldsymbol{\phi}_j\right)_\Omega,$$

$$\mathcal{G}_i = -\left(\boldsymbol{\phi}_i,\, (\boldsymbol{u}_c\cdot\boldsymbol{\nabla})\boldsymbol{u}_c\right)_\Omega.$$

B The Trust-Region Proper Orthogonal Decomposition algorithm

This appendix describes the TRPOD algorithm used in section 7.2.2.

TRPOD ALGORITHM. Initialization: Let η_1, η_2, γ_1, γ_2 and γ_3 be five positive constants such as $0 < \eta_1 < \eta_2 < 1$ and $0 < \gamma_1 \leq \gamma_2 < 1 \leq \gamma_3$. Let $\Delta^{(0)} > 0$ be an initial trust-region radius and $\boldsymbol{c}^{(0)}$ the initial control vector. Compute a set of snapshots $\mathcal{U}^{(0)}$ corresponding to the control $\boldsymbol{c}^{(0)}$ and estimate the value of the objective function $f(\boldsymbol{c}^{(0)})$. Set $k = 0$.

1. Compute a POD basis $\{\boldsymbol{\phi}_i^{(k)}\}_{i=1,\ldots,N_{POD}}$ using the snapshots $\mathcal{U}^{(k)}$ and derive a POD ROM of the controlled flow.

2. Compute the model function $m^{(k)}$ and solve the sub-problem

$$\boldsymbol{s}^{(k)} = \arg\min_{\boldsymbol{s}\in\mathbb{R}^n} m^{(k)}(\boldsymbol{c}^{(k)} + \boldsymbol{s}) \quad \text{subject to} \quad \|\boldsymbol{s}\| \leq \Delta^{(k)}.$$

3. Compute a snapshot set $\mathcal{U}^{(k+)}$ corresponding to the control $\boldsymbol{c}^{(k)} + \boldsymbol{s}^{(k)}$ and estimate the value of the objective function $f(\boldsymbol{c}^{(k)} + \boldsymbol{s}^{(k)})$. Determine $\rho^{(k)}$:

$$\rho^{(k)} = \frac{f(\boldsymbol{c}^{(k)} + \boldsymbol{s}^{(k)}) - f(\boldsymbol{c}^{(k)})}{m(\boldsymbol{c}^{(k)} + \boldsymbol{s}^{(k)}) - m(\boldsymbol{c}^{(k)})}.$$

4. Update the trust-region radius:

   - If $\rho^{(k)} \geq \eta_2$, the step is accepted: the iteration is successful. Set $\boldsymbol{c}^{(k+1)} = \boldsymbol{c}^{(k)} + \boldsymbol{s}^{(k)}$, $\mathcal{U}^{(k+1)} = \mathcal{U}^{(k+)}$ and choose $\Delta^{(k+1)} \in [\Delta^{(k)}, \gamma_3 \Delta^{(k)}]$. If a given criterion of convergence is verified, the algorithm is stopped, else, set $k = k + 1$ and return at the stage (1).
   - If $\eta_1 \leq \rho^{(k)} < \eta_2$, the step is accepted: the iteration is successful. Set $\boldsymbol{c}^{(k+1)} = \boldsymbol{c}^{(k)} + \boldsymbol{s}^{(k)}$, $\mathcal{U}^{(k+1)} = \mathcal{U}^{(k+)}$ and choose $\Delta^{(k+1)} \in [\gamma_2 \Delta^{(k)}, \Delta^{(k)}]$. If a given criterion of convergence is verified, the algorithm is stopped, else, set $k = k + 1$ and return at the stage (1).
   - If $\rho^{(k)} < \eta_1$, the step is refused: the iteration is unsuccessful. Set $\boldsymbol{c}^{(k+1)} = \boldsymbol{c}^{(k)}$, $\mathcal{U}^{(k+1)} = \mathcal{U}^{(k)}$ and choose $\Delta^{(k)} \in [\gamma_1 \Delta^{(k)}, \gamma_2 \Delta^{(k)}]$. Set $k = k + 1$ and return at the stage (2).

The usual parameters for the TRPOD algorithm are $\eta_1 = 0.25$ and $\eta_2 = 0.75$ for the criteria of performance, and $\gamma_1 = 0.25$, $\gamma_2 = 0.75$ and $\gamma_3 = 2$ for the criteria of actualization [50].

C Construction of the shift modes

The construction of the shift modes is based on a Gram-Schmidt orthonormalization procedure [75]. For example, the objective is to determine a mode of translation $\boldsymbol{\phi}_0^{I \to II}$ which represents the transition from the mean flow $\boldsymbol{\phi}_0^I$, associated to the dynamics I, to the mean flow $\boldsymbol{\phi}_0^{II}$, associated to the dynamics II, while preserving the orthonormality with the POD basis functions $\{\boldsymbol{\phi_i^I}\}_{i=0}^{N_{gal}}$ corresponding to the dynamics I.

The first stage consists in computing the translation vector $\boldsymbol{\phi}_0^{II} - \boldsymbol{\phi}_0^I$:

$$\boldsymbol{\phi}_a^{I \to II} = \boldsymbol{\phi}_0^{II} - \boldsymbol{\phi}_0^I.$$

By assumption, this mode of translation is supposed linearly independent of the POD modes $\{\boldsymbol{\phi_i^I}\}_{i=0}^{N_{gal}}$.

One then deduces from this mode, a new vector $\boldsymbol{\phi}_b^{I \to II}$ which supplements by construction the original POD basis in an orthogonal set:

$$\boldsymbol{\phi}_b^{I \to II} = \boldsymbol{\phi}_a^{I \to II} - \sum_{i=0}^{N_{gal}} \left(\boldsymbol{\phi}_a^{I \to II}, \boldsymbol{\phi}_i^I\right)_\Omega \boldsymbol{\phi}_i^I.$$

Finally, this vector is normalized

$$\boldsymbol{\phi}_0^{I \to II} = \frac{\boldsymbol{\phi}_b^{I \to II}}{\|\boldsymbol{\phi}_b^{I \to II}\|_\Omega}.$$

Formally, this mode can be considered as the $(N_{gal} + 1)$th expansion POD mode:

$$\boldsymbol{\phi}_{N_{gal}+1}^I \equiv \boldsymbol{\phi}_0^{I \to II}.$$

If it is desirable to include in the model another operating condition (dynamics III for example) then we set $N_{gal} = N_{gal} + 1$ and start again the procedure to determine a new shift mode $\boldsymbol{\phi}_0^{I \to III}$.

D Comparison of the computational costs: CPU and memory storage

As it was already mentioned, the solution of the TRPOD algorithm converges towards the solution of the optimization problem based on the high-order system. However, the TRPOD algorithm reduces significantly the numerical costs (CPU time and memory storage). In order to assess the performance of the TRPOD approach, the numerical costs involved in this study are compared to an estimation of those required when the full Navier-Stokes system are used as state equations. To make the comparison fair, it is necessary that the values of the parameters used to solve the Navier-Stokes equations are the same in both cases. As illustration, we consider that

- the time horizon $T_o = 20$,
- the time-step $\Delta t = 0.01$, and
- the number of vertices $N_v = 12\,000$.

For a gradient-type optimization method, an iteration of the optimization loop is made up of one determination of the cost function gradient and a linear search. To make the comparison relevant, we assumed that the number of iteration for the two optimization loops are the same. To simplify the estimation, we consider this number equal to one.

D.1 CPU time

In our approach, a POD ROM is used as state equations in the optimization loop. However, one Navier-Stokes resolution is required to determine the POD basis and it is necessary to build the POD model. To compare the CPU time, we assumed that the time required to solve the POD ROM is about 1% of that necessary to solve the Navier-Stokes equations. The same estimate can be made for the adjoint equations, for the optimality conditions and for the resolutions of the state equations carried out in the line search. Consequently, the CPU time required to solve the optimality system based on the POD ROM can be neglected in comparison to that necessary to the resolution of the optimality system based on the full-order model.

Finally, the following estimate of the CPU times can be made.

Full-order model

Let NS, ADJ and OC denote respectively the cost of resolution for the Navier-Stokes equations, the adjoint equations and the optimality conditions. In addition, let $N_{OC} \geq 1$ denotes the number of optimality conditions and $N_{LS} \geq 1$ the number of steps in the linear search.

The determination of the gradient of the cost functional requires the following resolutions:

- one time the Navier-Stokes equations, *i.e.* $1 \times$ NS,
- one time the adjoint equations, *i.e.* $1 \times$ ADJ $\simeq 1 \times$ NS,

- N_{OC} times the optimality conditions, *i.e.* $N_{OC} \times \text{OC} \simeq N_{OC} \times \text{NS}$.

The line search requires the resolution of:

- N_{LS} times the Navier-Stokes equations, *i.e.* $N_{LS} \times \text{NS}$.

The total CPU time required to solve one iteration of the optimization loop for the full-order model is approximately equal to $(2 + N_{OC} + N_{LS}) \times NS \geq 4 \times NS$.

POD ROM

Using the above assumptions, the CPU time that is required to solve one iteration of the optimization loop for the POD ROM is approximately equal to one resolution of the Navier-Stokes equations, *i.e.* $1 \times NS$.

Consequently, the computational time that is required to solve the optimality system based on the Navier-Stokes equations is at least equal to four times that necessary to solve the optimality system based on the POD ROM. Note that this factor of reduction can be much more important if there are many control parameters and if the number of search line to carry out is also important. However, since non equilibrium modes are added to the POD basis, one resolution of the Navier-Stokes equations is necessary for each mode, and the total CPU time used to solve the optimization problem by the TRPOD algorithm can then be slightly increased.

D.2 Memory storage

The main drawback of the optimal control theory in terms of memory storage is that we need to store the solutions of the state equations to solve the adjoint equations, and the solutions of the adjoint equations to solve the optimality conditions.

Full-order model

When the finite-element simulation is used to solve the optimality system over a time horizon T_o, we need to store the state and adjoint variables (two velocity components and the pressure) at every time step and for each vertex of the mesh, *i.e.* $N_{store} = (3 \times 2) \times N_v \times (T_o/\Delta_t) = 1.44\,10^8$ variables.

POD ROM

When the POD ROM is used, we only need to store the time evolution of the state variables and of the adjoint variables for $N_{gal} + N_{neq} + 1$ POD modes. In our study $N_{gal} = 14$ to represent 99.9% of the Relative Information Content and $N_{neq} = 5$. The coefficients appearing in the state equations must also be stored *i.e.* four linear coefficients ($\mathcal{A}$, $\mathcal{D}$, $\mathcal{E}$ and $\mathcal{G}$), two quadratic coefficients ($\mathcal{B}$ and $\mathcal{F}$) and one cubic coefficient ($\mathcal{C}$). The total number of variables to be stored is then $N_{store} = (20 \times 2) \times (T_o/\Delta_t) + (4 \times 20 + 2 \times 20^2 + 20^3) = 88\,880$.

If the POD ROM is used instead of the two dimensional Navier-Stokes equations to solve the optimization problem, the reduction factor of memory storage is equal to $1.44\,10^8/88\,880 \simeq 1\,600$.

Finally, if we decide to store the POD eigenfunctions to reconstruct later the velocity and pressure fields, it is then necessary to store $20 \times 12\,000 \times 3$ additional values and the storage reduction factor is now "only" equal to approximately 180.

References

[1] M. D. Gunzburger, Flow control, Springer, New York, 1995.

[2] M. D. Gunzburger, Introduction into mathematical aspects of flow control and optimization, in: Lecture series 1997-05 on inverse design and optimization methods, Von Kármán Institute for Fluid Dynamics, 1997.

[3] M. D. Gunzburger, Adjoint Equation-Based Methods for Control Problems in Incompressible, Viscous Flows, Flow, Turbulence and Combustion 65 (2000) 249–272.

[4] A. J. Booker, J. E. Dennis Jr., P. D. Frank, D. B. Serafini, V. Torczon, M. W. Trosset, A rigorous framework for optimization of expensive functions by surrogates, Structural Optimization 17 (1) (1999) 1–13.

[5] A. C. Antoulas, Approximation of Large-Scale Dynamical Systems, SIAM, 2005.

[6] K. Ito, S. S. Ravindran, A reduced-order method for simulation and control of fluid flows, J. Comp. Phys. 143 (1998) 403–425.

[7] J. L. Lumley, Atmospheric Turbulence and Wave Propagation. The structure of inhomogeneous turbulence, A.M. Yaglom & V.I. Tatarski, 1967, pp. 166–178.

[8] L. Sirovich, Turbulence and the dynamics of coherent structures, Quarterly of Applied Mathematics XLV (3) (1987) 561–590.

[9] K. E. Willcox, Reduced-order aerodynamic models for aeroelastic control of turbomachines, Ph.D. thesis, Massachusetts Institute of Technology (2000).

[10] J. Burkardt, M. D. Gunzburger, H.-C. Lee, Centroidal Voronoi Tessellation-Based Reduced-Order Modeling of Complex Systems, Tech. rep., Florida State University (2004).

[11] C. W. Rowley, Model reduction for fluids, using balanced proper orthogonal decomposition, Int. J. on Bifurcation and Chaos 15 (3) (2005) 997–1013.

[12] X. Ma, G. E. Karniadakis, A low-dimensional model for simulating three-dimensional cylinder flow, J. Fluid Mech. 458 (2002) 181–190.

[13] B. R. Noack, K. Afanasiev, M. Morzyński, G. Tadmor, F. Thiele, A hierarchy of low-dimensional models for the transient and post-transient cylinder wake, J. Fluid Mech. 497 (2003) 335–363.

[14] B. R. Noack, G. Tadmor, M. Morzyński, Low-dimensional models for feedback flow control. Part I: Empirical Galerkin models, in: 2nd AIAA Flow Control Conference, Portland, Oregon, U.S.A., June 28 – July 1, 2004, AIAA-Paper 2004-2408 (invited contribution).

[15] M. Bergmann, L. Cordier, J.-P. Brancher, Optimal rotary control of the cylinder wake using POD Reduced Order Model, Phys. Fluids 17 (9) (2005) 097101:1–21.

[16] W. R. Graham, J. Peraire, K. T. Tang, Optimal Control of Vortex Shedding Using Low Order Models. Part 1. Open-Loop Model Development, Int. J. for Numer. Meth. in Engrg. 44 (7) (1999a) 945–972.

[17] S. S. Ravindran, Reduced-order adaptive controllers for fluid flows using POD, J. of Scientific Computing 15 (4) (2000) 457–478.

[18] S. S. Ravindran, Adaptive Reduced-Order Controllers for a Thermal Flow System, SIAM Journal on Scientific Computing 23 (6) (2002) 1925–1943.

[19] M. Hinze, S. Volkwein, Proper Orthogonal Decomposition Surrogate Models for Nonlinear Dynamical Systems: Error Estimates and Suboptimal Control, Tech. rep., Preprint SFB609, Technische Universität Dresden (2004).

[20] C. H. K. Williamson, Vortex dynamics in the cylinder wake, Ann. Rev. Fluid. Mech. 28 (1996) 477–539.

[21] P. T. Tokumaru, P. E. Dimotakis, Rotary oscillatory control of a cylinder wake, J. Fluid Mech. 224 (1991) 77–90.

[22] X.-Y. Lu, J. Sato, A numerical study of flow past a rotationally oscillating circular cylinder, J. Fluids Struct. 10 (1996) 829–849.

[23] M. H. Chou, Synchronization of vortex shedding from a cylinder under rotary oscillation, Computers & Fluids 26 (1997) 755–774.

[24] S. J. Baek, H. J. Sung, Numerical simulation of the flow behind a rotary oscillating circular cylinder, Phys. Fluids 10 (4) (1998) 869–876.

[25] F. M. Mahfouz, H. M. Badr, Flow Structure in the Wake of a Rotationally Oscillating Cylinder, Journal of Fluids Engineering 122 (2) (2000) 290–301.

[26] S.-J. Baek, H. J. Sung, Quasi-periodicity in the wake of a rotationally oscillating cylinder, J. Fluid Mech. 408 (2000) 275–300.

[27] M. Cheng, Y. T. Chew, S. C. Luo, Numerical investigation of a rotationally oscillating cylinder in mean flow, J. Fluids Struct. 15 (2001) 981–1007.

[28] M. Cheng, G. R. Liu, K. Y. Lam, Numerical simulation of flow past a rotationally oscillating cylinder, Computers & Fluids 30 (2001) 365–392.

[29] S. Choi, H. Choi, S. Kang, Characteristics of flow over a rotationally oscillating cylinder at low Reynolds number, Phys. Fluids 14 (8) (2002) 2767–2777.

[30] B. Protas, J.-E. Wesfreid, Drag force in the open-loop control of the cylinder wake in the laminar regime, Phys. Fluids 14 (2) (2002) 810–826.

[31] N. Fujisawa, K. Ikemoto, K. Nagaja, Vortex shedding resonnance from a rotationally oscillating cylinder, J. Fluids Struct. 12 (1998) 1041–1053.

[32] N. Fujisawa, Y. Kawaji, K. Ikemoto, Feedback control of vortex shedding from a circular cylinder by rotational oscillations, J. Fluids Struct. 15 (2001) 23–37.

[33] S. Goujon-Durand, J.-E. Wesfreid, P. Jenffer, Contrôle actif du sillage autour d'un cylindre oscillant, in: 15th French Congress of Mechanics, Nancy, Sept. 3 – 7, 2001.

[34] B. Thiria, S. Goujon-Durand, J.-E. Wesfreid, Wake of a cylinder performing rotary oscillations, Submitted to J. Fluid Mech.

[35] F. Abergel, R. Temam, On some control problems in fluid mechanics, Theoret. Comput. Fluid Dynamics 1 (1990) 303.

[36] T. R. Bewley, Flow control: new challenges for a new Renaissance, Progress in Aerospace Sciences 37 (2001) 21–58.

[37] T. R. Bewley, The emerging roles of model-based control theory in fluid mechanics, in: Advances in Turbulence IX, 2002, ninth European Turbulence Conference.

[38] J.-W. He, R. Glowinski, R. Metcalfe, A. Nordlander, J. Périaux, Active control and drag optimization for flow past a circular cylinder. Part 1. Oscillatory cylinder rotation, J. Comp. Phys. 163 (2000) 83–117.

[39] C. Homescu, I. M. Navon, Z. Li, Suppression of vortex shedding for flow around a circular cylinder using optimal control, Int. J. Numer. Meth. Fluids 38 (2002) 43–69.

[40] B. Protas, A. Styczek, Optimal rotary control of the cylinder wake in the laminar regime, Phys. Fluids 14 (7) (2002) 2073–2087.

[41] T. R. Bewley, P. Moin, R. Temam, DNS-based predictive control of turbulence: an optimal benchmark for feedback algorithms, J. Fluid Mech. 447 (2001) 179–225.

[42] Y. Chang, Approximate models for optimal control of turbulent channel flow, Ph.D. thesis, Rice university (2000).

[43] M. Wei, J. B. Freund, A noise-controlled free shear flow, J. Fluid Mech. 546 (2006) 123 – 152.

[44] N. Alexandrov, J. E. Dennis Jr, R. M. Lewis, V. Torczon, A Trust Region framework for managing the use of approximation models in optimization, Icase report 97-50.

[45] M. Bergmann, L. Cordier, J.-P. Brancher, On the power used to control the circular cylinder drag by rotary oscillations, Phys. Fluids 18 (8) (2006) 088103:1–4.

[46] B. R. Noack, H. Eckelmann, A global stability analysis of the steady and periodic cylinder wake, J. Fluid Mech. 270 (1994) 297–330.

[47] D. Barkley, R. D. Henderson, Three-dimensional Floquet stability analysis of the wake of a circular cylinder, J. Fluid Mech. 322 (1996) 215–241.

[48] L. Cordier, M. Bergmann, Proper Orthogonal Decomposition: an overview, in: Lecture series 2002-04 on post-processing of experimental and numerical data, Von Kármán Institute for Fluid Dynamics, 2002.

[49] W. R. Graham, J. Peraire, K. T. Tang, Optimal Control of Vortex Shedding Using Low Order Models. Part 2: Model-based control, Int. J. for Numer. Meth. in Engrg. 44 (7) (1999b) 973–990.

[50] M. Fahl, Trust-region methods for flow control based on Reduced Order Modeling, Ph.D. thesis, Trier university (2000).

[51] J. Nocedal, S. J. Wright, Numerical Optimization, Springer series in operations research, 1999.

[52] G. Jin, M. Braza, A Nonreflecting Outlet Boundary Condition for Incompressible Unsteady Navier-Stokes Calculations, J. Comp. Phys. 107 (2) (1993) 239–253.

[53] L. Cordier, M. Bergmann, Two typical applications of POD: coherent structures eduction and reduced order modelling, in: Lecture series 2002-04 on post-processing of experimental and numerical data, Von Kármán Institute for Fluid Dynamics, 2002.

[54] M. Bergmann, Optimisation aérodynamique par réduction de modèle POD et contrôle optimal. Application au sillage laminaire d'un cylindre circulaire., Ph.D. thesis, Institut National Polytechnique de Lorraine, Nancy, France (2004).

[55] B. Protas, J.-E. Wesfreid, On the relation between the global modes and the spectra of drag and lift in periodic wake flows, C.R. Mécanique 331 (2003) 49–54.

[56] M. Braza, P. Chassaing, H. Ha Minh, Numerical study and physical analysis of the pressure and velocity fields in the near wake of a circular cylinder, J. Fluid Mech. 165 (1986) 79.

[57] R. D. Henderson, Nonlinear dynamics and pattern formation in turbulent wake transition, J. Fluid Mech. 352 (1997) 65–112.

[58] M. Bergmann, L. Cordier, J.-P. Brancher, On the generation of a reverse Von Kármán street for the controlled cylinder wake in the laminar regime, Phys. Fluids 18 (2) (2006) 028101:1–4.

[59] P. Holmes, J. L. Lumley, G. Berkooz, Turbulence, Coherent Structures, Dynamical Systems and Symmetry, Cambridge Monographs on Mechanics, 1996.

[60] K. Zhou, J. C. Doyle, K. Glover, Robust and optimal control, Prentice Hall, 1996.

[61] B. R. Noack, P. Papas, P. A. Monkewitz, The need for a pressure-term representation in empirical galerkin models of incompressible shear-flows, J. Fluid Mech. 523 (2005) 339–365.

[62] B. Galletti, C.-H. Bruneau, L. Zannetti, A. Iollo, Low-order modelling of laminar flow regimes past a confined square cylinder, J. Fluid Mech. 503 (2004) 161–170.

[63] M. Couplet, C. Basdevant, P. Sagaut, Calibrated reduced-order POD-Galerkin system for fluid flow modelling, J. Comp. Phys. 207 (2005) 192–220.

[64] S. Sirisup, G. E. Karniadakis, A spectral viscosity method for correcting the long-term behavior of POD model, J. Comp. Phys. 194 (2004) 92–116.

[65] P. Sagaut, Large-eddy simulation for incompressible flows - An introduction, Springer-Verlag, 2005.

[66] G. S. Karamanos, G. E. Karniadakis, A spectral vanishing viscosity method for Large Eddy Simulations, J. Comp. Phys. 162 (2000) 22–50.

[67] E. Arian, M. Fahl, E. W. Sachs, Trust-Region Proper Orthogonal Decomposition for Flow Control, Icase report 2000-25.

[68] A. R. Conn, N. I. M. Gould, P. L. Toint, Trust-region methods, SIAM, Philadelphia, 2000.

[69] P. L. Toint, Global convergence of a class of trust-region methods for nonconvex minimization in Hilbert space, IMA J. Numer. Anal. 8 (2) (1988) 231–252.

[70] D. Rempfer, Investigations of boundary layer transition via Galerkin Projections on Empirical Eigenfunctions, Phys. Fluids 8 (1) (1996) 175–188.

[71] A. E. Deane, I. G. Kevrekidis, G. E. Karniadakis, S. A. Orszag, Low-dimensional models for complex geometry flows: Application to grooved channels and circular cylinders, Phys. Fluids 3 (10) (1991) 2337–2354.

[72] D. Rempfer, H. F. Fasel, Evolution of three-dimensional coherent structures in a flat-plate boundary layer, J. Fluid Mech. 260 (1994) 351–375.

[73] K. Afanasiev, M. Hinze, Adaptive control of a wake flow using Proper Orthogonal Decomposition, in: Shape Optimization and Optimal Design, Lecture Notes in Pure and Applied Mathematics, Vol. 216, Marcel Dekker, 2001.

[74] C. Homescu, L. R. Petzold, R. Serban, Error Estimation for Reduced Order Models of Dynamical Systems, Tech. rep., Lawrence Livermore National Laboratory (2003).

[75] G. H. Golub, C. F. van Loan, Matrix Computations, Johns Hopkins University Press, 1996.

Contents

Centre de recherche INRIA Bordeaux – Sud Ouest
Domaine Universitaire - 351, cours de la Libération - 33405 Talence Cedex (France)

Centre de recherche INRIA Grenoble – Rhône-Alpes : 655, avenue de l'Europe - 38334 Montbonnot Saint-Ismier
Centre de recherche INRIA Lille – Nord Europe : Parc Scientifique de la Haute Borne - 40, avenue Halley - 59650 Villeneuve d'Ascq
Centre de recherche INRIA Nancy – Grand Est : LORIA, Technopôle de Nancy-Brabois - Campus scientifique
615, rue du Jardin Botanique - BP 101 - 54602 Villers-lès-Nancy Cedex
Centre de recherche INRIA Paris – Rocquencourt : Domaine de Voluceau - Rocquencourt - BP 105 - 78153 Le Chesnay Cedex
Centre de recherche INRIA Rennes – Bretagne Atlantique : IRISA, Campus universitaire de Beaulieu - 35042 Rennes Cedex
Centre de recherche INRIA Saclay – Île-de-France : Parc Orsay Université - ZAC des Vignes : 4, rue Jacques Monod - 91893 Orsay Cedex
Centre de recherche INRIA Sophia Antipolis – Méditerranée : 2004, route des Lucioles - BP 93 - 06902 Sophia Antipolis Cedex

Éditeur
INRIA - Domaine de Voluceau - Rocquencourt, BP 105 - 78153 Le Chesnay Cedex (France)
http://www.inria.fr
ISSN 0249-6399